Inorganic Chemistry

Article

Cite This: Inorg. Chem. 2017, 56, 11819-11836

pubs.acs.org/IC

A Restricted Open Configuration Interaction with Singles Method To Calculate Valence-to-Core Resonant X-ray Emission Spectra: A Case Study

Dimitrios Maganas, Serena DeBeer, and Frank Neese*

Max Planck Institute for Chemical Energy Conversion, Stiftstrasse 34−36, D-45470 Mülheim an der Ruhr, Germany

Supporting Information

ABSTRACT: In this work, a new protocol for the calculation of valence-to-core resonant X-ray emission (VtC RXES) spectra is introduced. The approach is based on the previously developed restricted open configuration interaction with singles (ROCIS) method and its parametrized version, based on a ground-state Kohn−Sham determinant (DFT/ROCIS) method. The ROCIS approach has the following features: (1) In the first step approximation, many-particle eigenstates are calculated in which the total spin is retained as a good quantum number. (2) The ground state with total spin S and excited states with spin $S' = S, S \pm 1$, are obtained. (3) These states have a qualitatively correct multiplet structure. (4) Quasi-degenerate perturbation theory is used to treat the spin−orbit coupling operator variationally at the many-particle level. (5) Transition moments are obtained between the relativistic many-particle states. The method has shown great potential in the field of X-ray spectroscopy, in particular in the field of transition-metal L-edge, which cannot be described correctly with particle−hole theories. In this work, the method is extended to the calculation of resonant VtC RXES [alternatively referred to as 1s-VtC resonant inelastic X-ray scattering (RIXS)] spectra. The complete Kramers−Dirac−Heisenerg equation is taken into account. Thus, state interference effects are treated naturally within this protocol. As a first application of this protocol, a computational study on the previously reported VtC RXES plane on a molecular managanese(V) complex is performed. Starting from conventional X-ray absorption spectra (XAS), we present a systematic study that involves calculations and electronic structure analysis of both the XAS and non-resonant and resonant VtC XES spectra. The very good agreement between theory and experiment, observed in all cases, allows us to unravel the complicated intensity mechanism of these spectroscopic techniques as a synergic function of state polarization and interference effects. In general, intense features in the RIXS spectra originate from absorption and emission processes that involve nonorthogonal transition moments. We also present a graphical method to determine the sign of the interference contributions.

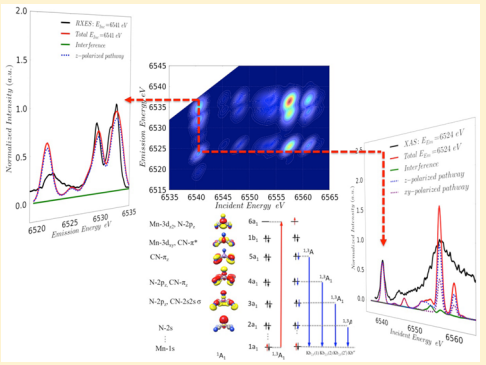

1. INTRODUCTION

Analysis of electronic spectra of chemical systems requires that an unambiguous relationship between the spectral observables and electronic structure be established. In this respect, X-ray-based techniques, such as X-ray absorption (XAS) and X-ray emission (XES) spectroscopies, play a significant role because they operate in an element-specific fashion and probe the electronic structure of the absorbing atom.[1−9] A drawback of XAS and XES, however, is that both methods are intrinsically bulk probes and are thus limited in their selectivity. As a result, there has been much recent interest in two-dimensional X-ray spectroscopic measurements in which both XAS and XES are combined within the same experiment. In such a measurement, one measures XAS on the x axis and follows the emission process of interest in the y axis. This results in a so-called resonant XES (RXES) or resonant inelastic X-ray scattering (RIXS) plane. RXES planes are typically labeled according to the core level from which an electron is excited, followed by the level from which the electron decays. For instance, in the hard X-ray regime, one may follow 1s2p, 1s3p, or 1s valence (or VtC) RXES processes. These correspond to monitoring of the Kα, Kβ, and VtC XES processes, respectively. We note that, in analogy to other well-known two-dimensional spectroscopies (e.g., 2D NMR or electron nuclear double resonance spectroscopy) in RXES, both experimental dimensions carry useful chemical information. Along the emission axis at constant incident energy, one detects RXES spectra, while along the incident axis at constant emission energy, the respective high-energy-resolution fluorescence-detected (HERFD) XAS spectra are detected.

In recent years, experimentalists have shown that oxidation-state- and spin-state-selective XAS data can be obtained from 1s3p RXES.[10−13] These studies emphasize the added selectivity of such an approach. Recently, we have reported VtC RXES data on a series of manganese compounds.[14] These experiments combine XAS with ligand-sensitive VtC XES and thus provided the first experimental steps toward "ligand-selective

Received: July 17, 2017
Published: September 18, 2017

DOI: 10.1021/acs.inorgchem.7b01810
Inorg. Chem. 2017, 56, 11819−11836

XAS". Dramatic variations in the VtC-detected HERFD XAS spectra were observed as a function of the VtC emission energy. However, at the time of publication, the available theoretical protocols did not allow for an understanding of the dramatic spectral changes that occurred.

Herein, we demonstrate that VtC RXES spectra can be reproduced by utilizing a rigorous wave-function-based computational protocol. Importantly, we show that the intensity mechanism for VtC RXES is extremely sensitive to polarization selection rules. Hence, the present findings demonstrate that VtC RXES may be used to obtain polarization-dependent information from isotropic samples. Finally, we emphasize that the developed computational protocols, while applied here only for VtC RXES, should be readily applicable for the calculation of a wide range of RXES/RIXS processes.

2. COMPUTATIONAL CHALLENGES IN THE CALCULATION ON VTC RXES SPECTRA

Before the computational details are presented, it is useful to first briefly discuss the challenges associated with calculating VtC RXES and VtC-detected HERFD XAS spectra.

As can be seen in Scheme 1 even for relatively simple cases dealing, for example, with d^0 transition-metal complexes, in addition to ligand-field and covalency effects, one must consider the open-shell intermediate $M(n-2)s^1L(n-1)s^2L(n-1)p^6M(n)d^{m+1}$ and final $M(n-2)s^2L(n-1)s^1L(n-1)p^6M(n)d^{m+1}$ $M(n-2)s^2L(n-1)s^2L(n-1)p^5M(n)d^{m+1}$ state configurations, where M and L refer to metal- and ligand-based orbitals, respectively. In general, the configurations involved in RIXS and VtC RXES processes may result in many intermediate- and final-state multiplets with complicated electronic structures. In addition, open-core-level metal p shells and/or metal d shells may be subject to spin−orbit coupling (SOC), which strongly mixes the "nonrelativistic" final states. Thus, a satisfactory first-principles approach needs to (a) generate all possible electronic configurations involved in the resonant excitation process and properly construct spin-coupled configuration state functions (CSFs), (b) account for dynamic electron correlation in order to ensure a correct relative energetic positioning of the various multiplets, (c) properly describe the SOC between these multiplets, and (d) ensure that metal−ligand (M−L) covalency is correctly treated. Clearly, density functional theory (DFT) and various derived particle−hole theories fall short of meeting these requirements because neither can they span the correct space of the intermediate or final states nor can they explicitly represent the various members of each spin multiplet. Hence, in our opinion, the only choice to arrive at a physically sound description of RIXS spectra is to resort to wave-function-based methodologies.

Scheme 1. Schematic Representation of the Ground/Initial, Intermediate, and Final States ($|I\rangle$, $|V\rangle$, and $|F\rangle$) along with the Dominating Electron Configurations (M = Metal; L = Ligand) Involved in the VtC RXES Process

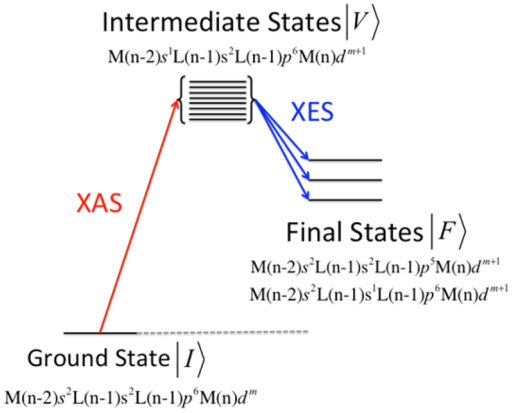

In general, problems of such complexity can be most adequately treated with multireference ab initio wave-function methodologies.[15−17] In these approaches, the necessary low-lying intermediate and final states reached by experiment are determined and used to construct the multiplet structure on an equal footing through a multiconfigurational treatment. However, in VtC RXES, both core and valence electrons must be correlated simultaneously; hence, the resulting active space, as well as the required states to be treated within the configuration interaction approach, becomes prohibitively large. This drastically narrows down the applicability of most established methods that would be able to address such problems in a transparent and realistic fashion, namely, the complete-active-space configuration interaction or multireference configuration interaction methods. Nevertheless, such methods have been proven to be extremely useful in describing the complex intensity mechanisms that give rise to VtC RXES spectra of small gaseous molecules.[18]

One way to achieve a drastic reduction of the computational effort is to focus attention toward restricted active spaces, in which the configuration interaction space is truncated to essentially only include the XAS and RXES or VtC RXES excitation spaces. Recently, restricted-active-space configuration interaction methods have attracted attention because they have performed well for the calculation of non-resonant XES as well as the 2p3d and 1s2p RXES spectra for iron, cobalt, and nickel complexes.[15,17,19−25] Additional complexity arises from the high number of the intermediate and final states to be determined for an actual VtC RXES plane calculation. In fact, protocols like the one described above would be adequate to treat the metal 2p3d, 1s3d, or 1s2p RIXS problems, where the excitation space, by definition, is restricted to the metal d−d manifold and the metal core holes. On the other hand, treatment of the 1s2p VtC RXES problem, where the VtC excitation space spans the entire manifold between the metal d and p and ligand p and s orbitals, is a rather challenging problem for active-space-based methods.

In our development of the wavefunction methods that are tailored to X-ray spectroscopy, we have extended the applicability of the DFT/restricted open configuration interaction with singles (DFT/ROCIS) method to treat various VtC RXES spectra. Originally, the ROCIS method was introduced as an alternative approach to treating the transition-metal L-edge problem. The method can treat classes of molecular systems from transition-metal compounds up to polymetallic clusters with several hundreds of atoms.[26,27] The DFT/ROCIS method is based on a high-spin-coupled restricted open-shell determinant. Thus, systems with multiconfigurational or orbitally degenerate ground states (e.g., antiferromagnetically aligned solids) cannot presently be treated. The implementation and application of this methodology to treat the metal L-edge problem of various closed- and open-shell compounds and polymetallic clusters have recently been explored.[5,26,28]

As the first application study of the VtC RXES DFT/ROCIS protocol, we have chosen to treat the 1s2p VtC RXES problem

DOI: 10.1021/acs.inorgchem.7b01810
Inorg. Chem. 2017, 56, 11819−11836

in the case study of $[Mn^{V}N(CN)_4]^{2-}$. Aiming at further insight from wave-function-based theories, we present herein a detailed VtC RXES study of the $(PPh_4)_2[MnN(CN)_4]$ complex by using the newly developed DFT/ROCIS VtC RXES protocol.

3. THEORY

3.1. DFT/ROCIS. Prior to the calculation of the VtC RXES spectra, one has to obtain a solution of the DFT/ROCIS wave function. The DFT/ROCIS approach starts from a high-spin open-shell determinant built from a set of DFT orbitals. One then obtains the DFT/ROCIS wave function by applying a spin-adapted excitation operator to this reference determinant and solving the secular problem. Thus, the DFT/ROCIS wave function is written as a linear combination of the zeroth-order wave function and excited spin-adapted CSFs $|\Phi_I\rangle$.

The restricted high-spin open-shell reference determinant ($|0^{SS}\rangle$ refers to the ground-state reference determinant with total spin S and spin-projection quantum number $M(S)$ written as

$$|0^{SS}\rangle = |\psi_1\bar{\psi}_1,\ ...,\ \psi_n\bar{\psi}_n\psi_t\psi_u,\ ...| \tag{1}$$

$\psi_i(\mathbf{r})$ is a molecular orbital (MO), and an overbar refers to occupation with a spin-down electron; singly occupied MOs are referred to as ψ_t, ψ_u, ... Excited CSFs are constructed by applying spin-traced excitation operators $E_p^q = a_{q\beta}^+ a_{p\beta} + a_{q\alpha}^+ a_{p\alpha}$ as well as spin-flip operators $S_p^{q+} = a_{q\alpha}^+ a_{p\beta}$ and $S_p^{q-} = a_{q\beta}^+ a_{p\alpha}$. Here p and q are general orbital labels and α and β refer to spin cases, while a^+ and a refer to standard Fermion creation and annihilation operators to $|0^{SS}\rangle$. In this way, one arrives at a set of CSFs for which the total spin is a good quantum number and that spans most of the multiplets available to a given system. The coefficients with which the CSFs enter into the ROCIS wave function are determined variationally through the solution of the ROCIS eigenvalue problem:

$$H_{BO}\Psi = E\Psi \tag{2}$$

With matrix elements $H_{IJ} = \langle\Phi_I|H_{BO}|\Phi_J\rangle$ and $|\psi_I^{SS}\rangle = \sum_\mu C_{\mu I}|\Phi_\mu^{SS}\rangle$. The Born–Oppenheimer operator is

$$H_{BO} = \sum_{pq} h_{pq}E_p^q + \frac{1}{2}\sum_{pqrs}(pq|rs)(E_p^qE_r^s - \delta_{pr}E_q^s) \tag{3}$$

where h_{pq} refers to matrix elements of the one-electron operator that may or may not be supplemented with matrix elements of an external potential (e.g., modeling a crystal environment) and a scalar relativistic potential, for example, provided by the second-order Douglas–Kroll–Hess (DKH[29−33]) or zeroth order for relativistic effects (ZORA[34−36]) methods; $(pq|rs)$ are the two-electron repulsion integrals in Mulliken (charge-cloud) notation. The excited-state configurations are constructed by performing single excitations relative to each CSF in the reference space. Thus, the ROCIS wave functions with total spin $S' = S, S \pm 1$, are given by eqs 4–6:

$$|\Psi_I^{SS}\rangle = c_{0I}|0^{SS}\rangle + \sum_{it} c_{i;I}^t|\Phi_i^t\rangle + \sum_{ia} c_{i;I}^a|\Phi_i^a\rangle + \sum_{ita} c_{ti;I}^{at}|\Phi_{ti}^{at}\rangle + \sum_{itwa} c_{wi;I}^{at}|\Phi_{wi}^{at}\rangle \tag{4}$$

$$|\Psi_I^{S-1,S-1}\rangle = \sum_{it} c_{i;I}^t|\Phi_i^{t(-)}\rangle + \sum_{it} c_{t;I}^a|\Phi_t^{a(-)}\rangle + \sum_{ia} c_{i;I}^a|\Phi_i^{a(-)}\rangle \tag{5}$$

$$|\Psi_I^{S+1,S+1}\rangle = \sum_{ia} c_{i;I}^a|\Phi_i^{a(+)}\rangle \tag{6}$$

where throughout uppercase labels refer to many-electron quantities and lowercase labels to one-electron quantities. Indices i, j, k, and l refer to doubly occupied orbitals in the reference determinant, t, u, v, and w to the singly occupied ones, and a, b, c, and d to the virtual orbitals, while p, q, r, and s refer to general orbitals.

The eigenstates of the spin-free operator are used to expand the relativistic eigenstates in the presence of the SOC by solving the quasi-degenerate eigenvalue problem:

With the matrix elements:

$$\langle\Psi_I^{SM}|H_{BO} + H_{SOC}|\Psi_J^{S'M'}\rangle = \delta_{IJ}\delta_{SS'}\delta_{MM'}E_I^S + \sum_{m=0,\pm1}(-1)^m\begin{pmatrix} S' & 1 & S \\ M' & m & M \end{pmatrix}\langle\Psi_I^{SS}\|H_{-m}^{SOC}\|\Psi_J^{SS}\rangle \tag{7}$$

Here, $\begin{pmatrix} S' & 1 & S \\ M' & m & M \end{pmatrix}$ is a Clebsch–Gordon coefficient and $\langle\Psi_I^{SS}\|H_{-m}^{SOC}\|\Psi_J^{SS}\rangle$ is a reduced matrix element of the spin–orbit operator discussed in ref 14. For the latter, we make use of the spin–orbit mean-field operator discussed in ref 14:

$$H_{SOC} = \sum_i \mathbf{h}^{SOC}(\mathbf{x}_i)\ \mathbf{s}(i) \tag{8}$$

where $\mathbf{x}_i$ and $\mathbf{s}(i)$ refer to the coordinates and spin operators of electron i, respectively. The effective mean-field one-electron spin–orbit operator $\mathbf{h}^{SOC}(\mathbf{x}_i)$ contains one- and two-electron SOC integrals and also incorporates the spin–other orbit interaction.[37] It has been repeatedly shown to provide a faithful description of the SOC effects.[26−28,38] In the presence of a scalar-relativistic potential, picture change effects on the SOC operator are included.

Further details on the DFT/ROCIS method, working equations, and further implementation details describing how ROCIS and DFT/ROCIS are implemented in the *ORCA* computational package are given elsewhere.[39]

3.2. VtC RXES. The VtC RXES implementation in the DFT/ROCIS framework is based on the direct application of the Kramers–Dirac–Heisenerg (KDH) expression.[40] In analogy to Raman scattering,[41] X-ray scattering is described by second-order time-dependent perturbation theory. The polarizability tensor $|\alpha_{\rho\lambda}|(E_{ex}E_{em})|$ for inelastic scattering is given by

$$|\alpha_{\rho\lambda}(E_{ex}, E_{em})|_{total}^2 = \sum_F\left|\sum_V \frac{\langle F|m_\rho|V\rangle\langle V|m_\lambda|I\rangle}{E_{VI} - E_{em} - i\frac{1}{2}\Gamma_V}\right|^2 \times\left\{\frac{\Gamma_F}{(E_{FV} - E_{ex} + E_{em})^2 + \frac{1}{4}\Gamma_F^2}\right\} \tag{9}$$

where $|I\rangle$ is the initial state, $|V\rangle$ is the intermediate state, and $|F\rangle$ is the final state. The energies E_{ex} and E_{em} correspond to the incident excitation and emission energy, respectively, while E_{VI} and E_{FV} are the transition energies between the intermediate state and the initial and final states, respectively. The parameters Γ_V and Γ_F are the line broadenings arising from the lifetimes of the intermediate and final states, respectively. They are usually treated as phenomenological parameters and

DOI: 10.1021/acs.inorgchem.7b01810
Inorg. Chem. 2017, 56, 11819–11836

implicitly incorporate a variety of broadening mechanisms, and m is a component of the electric-dipole transition operator (in atomic units $\mathbf{m} = -\sum_i \mathbf{r}_i + \sum_A Z_A \mathbf{R}_A$) where r_i is the position operator for the ith electron and A sums over nuclei with charges Z_A at positions $\mathbf{R}_A$. A visual representation of eq 9 is depicted in Scheme 1.

Inspection of eq 9 shows that (1) the dominating product terms will arise between matrix elements with nonorthogonal transition dipole moments and (2) the contributions from all of the intermediate states have to be summed before squaring. Because the individual terms can be positive or negative, counterintuitive interference contributions may arise.

If, on the other hand, E_{ex} is tuned right into resonance with an intermediate state V, this one state will dominate the sum and, thus, eq 9 can be simplified to eqs 10 and 11.

$$|\alpha_{\rho\lambda}(E_{ex}, E_{em}, V)|_{resonant}^{2} = \sum_F |\langle F|m_\rho|V\rangle|^2 |\langle V|m_\lambda|I\rangle|^2 f(E_{VI}, E_{FV}, E_{ex}, E_{em}, \Gamma_V, \Gamma_F) \tag{10}$$

$$f(E_{VI}, E_{FV}, E_{ex}, E_{em}, \Gamma_V, \Gamma_F) = \frac{1}{2\pi}\left[\frac{\Gamma_V}{(E_{VI} - E_{ex})^2 + \frac{1}{4}\Gamma_V^2}\right] \times \left[\frac{\Gamma_F}{(E_{FV} - E_{ex} + E_{em})^2 + \frac{1}{4}\Gamma_F^2}\right] \tag{11}$$

Summing $|\alpha_{\rho\lambda}(E_{ex}E_{em})|_{resonant}^{2}$ over all intermediate states gives the "direct", e.g., interference-free, approximation to the full scattering tensor:

$$|\alpha_{\rho\lambda}(E_{VI}, E_{em})|_{direct}^{2} = \sum_V |\alpha_{\rho\lambda}(E_{VI}, E_{em}, V)|_{resonant}^{2} \tag{12}$$

The resonance scattering cross section for the total and direct cases, averaged over all orientations of the molecule and integrated over all directions and polarizations of scattered radiation, is given in eqs 13 and 14:

$$\sigma_{RXES}^{direct}(E_{ex}, E_{em}) = \frac{8\pi E_{em}^{3} E_{ex}}{9c^4} \sum_{\rho,\lambda=x,y,z} |\alpha_{\rho\lambda}(E_{ex}, E_{em})|_{direct}^{2} \tag{13}$$

$$\sigma_{RXES}^{total}(E_{ex}, E_{em}) = \frac{8\pi E_{em}^{3} E_{ex}}{9c^4} \sum_{\rho,\lambda=x,y,z} |\alpha_{\rho\lambda}(E_{ex}, E_{em})|_{total}^{2} \tag{14}$$

where c is the speed of light (~137 in atomic units) and 4π is the solid angle.

Interference effects can be then derived in a straightforward way from eq 15.

$$\sigma_{RXES}^{interference}(E_{ex}, E_{em}) = \sigma_{RXES}^{total}(E_{ex}, E_{em}) - \sigma_{RXES}^{direct}(E_{ex}, E_{em}) \tag{15}$$

The actual experimental practice of presenting the data in terms of "energy transfer", e.g., relative to the energy of the incident radiation, is provided as a user choice in the present implementation. Moreover, other line shapes can be considered, in particular, the convolution of two Gaussians rather than two Lorenzians. Note that the respective XAS and nonresonant XES experiments can be analogously described by the absorption cross section given in eq 16.

$$\sigma_{XAS/XES}(E_{ex}) = \frac{4\pi}{3c} E_{ex} \sum_F \sum_{\rho=x,y,z} \frac{|\langle F|m_\rho|I\rangle|^2 \Gamma}{(E_{FI} - E_{ex}) - \frac{1}{4}\Gamma^2} \tag{16}$$

3.3. Natural Transition/Natural Difference Orbitals. Because analysis of the calculated many-particle spectra in terms of predominant single-electron excitations may become extremely complicated, we introduce herein the machinery of natural transition and natural difference orbitals.

Within the ROCIS method, the calculated transition densities between two general ROCIS states are given by eq 17.

$$\rho_{pq}^{IF} = \langle \Psi_F | E_p^q | \Psi_I \rangle$$
$$\rho_{pq}^{IF} = \sum_{\kappa,\lambda}^{CI\ basis} C_{\lambda F}^{*} C_{\kappa I} \langle \lambda | E_p^q | \kappa \rangle \tag{17}$$

Hence, one can evaluate the transition densities between the ground and excited states ρ_{pq}^{0F} as well as the corresponding difference densities $\rho_{pq}^{FF} - \rho_{pq}^{00}$. These densities are then diagonalized in the donor and acceptor space to provide the corresponding donor and acceptor natural orbital pairs dominating the state.

3.4. One-Electron DFT Approach. An alternative and far more simplistic approach to XAS, VtC XES, and VtC RXES intensities is provided by the one-electron approach based on the DFT orbitals and orbital energies. The method is perhaps best thought of as a simplification of the time-dependent DFT (TD-DFT) approach. It is frequently the case that TD-DFT eigenvectors in the Tamm−Dancoff (TDA) approximation are dominated by a single particle−hole excitation. Furthermore, as long as there is no HF exchange in the functional, the orbital energy difference provides a valid zeroth-order approximation to the transition energy. Hence, rather than solving the TD-DFT/TDA problem for all possible states, one simply approximates these states by elementary particle−hole excitations. This approach has the obvious drawbacks that (1) it does not properly treat the multiplet structure of the final state manifold and (2) it ignores any possible strong state mixing and lacks electronic relaxation. Finally, (3) in the case of VtC RXES, only the direct processes are treated, while interference effects are omitted. The benefit of the treatment is its simplicity, efficiency, and transparency.

In a nutshell, the initial, intermediate, and final states can be expressed in a single determinantal form as

$$|I\rangle = |i, \ldots, j, \ldots, n|$$
$$|V\rangle = |a, \ldots, j, \ldots, n|$$
$$|F\rangle = |a, \ldots, i, \ldots, n| \tag{18}$$

where i represents an occupied core orbital, a is an unoccupied orbital, and j is another core orbital.

The absorption cross section for the XAS and XES processes turns into a simple sum over orbital donor−acceptor (particle−hole) pairs:

$$\sigma_{XAS}(E_{ex}) = \frac{4\pi}{3c} E_{ex} \sum_{i_\sigma a_\sigma} \sum_{\rho=x,y,z} \frac{|\langle a_\sigma|m_p|i_\sigma\rangle|^2 \Gamma}{(\varepsilon_a^\sigma - \varepsilon_i^\sigma - E_{ex}) + \frac{1}{4}\Gamma^2} \tag{19}$$

DOI: 10.1021/acs.inorgchem.7b01810
Inorg. Chem. 2017, 56, 11819−11836

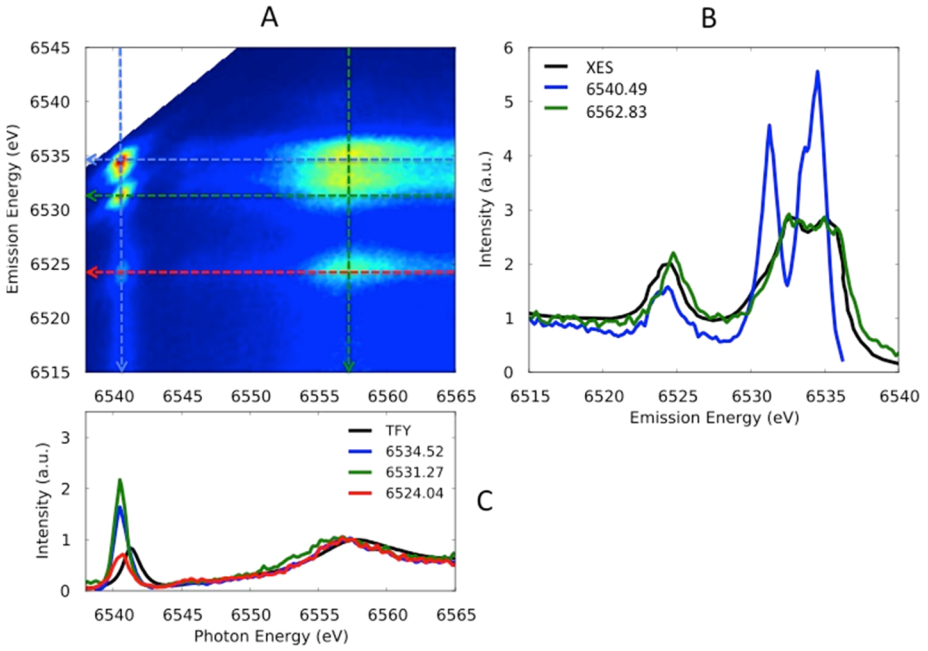

Figure 1. (A) Experimental RIXS plane for $(PPh_4)_2$ $[Mn(CN)_4N]$. (B) Preedge (blue) and edge (green) detected Kβ'' and K$\beta_{2,5}$(1,2) features. (C) Kβ''- (red), Kβ2,5(1) (1)- (green), and Kβ2,5(1) (2)- (blue) detected XAS spectra. Black lines indicate the corresponding XES and TFY XAS spectra.

$$\sigma_{XAS}(E_{ex}) = \frac{4\pi}{3c}E_{ex}\sum_{j_\sigma a_\sigma}\sum_{\rho=x,y,z}\frac{|\langle a_\sigma|m_\rho|j_\sigma\rangle|^2\Gamma}{(\varepsilon_a^\sigma - \varepsilon_j^\sigma - E_{ex}) + \frac{1}{4}\Gamma^2} \tag{20}$$

while the polarizability tensor is given by the triple sum over orbitals:

$$\sigma_{RXES}^{direct}(E_{ex}, E_{sc}) = \frac{8\pi E_{em}{}^3E_{ex}}{9c^4}\times \sum_{i_\sigma}\sum_{j_\sigma}\sum_{a_\sigma} f(\varepsilon_a^\sigma - \varepsilon_i^\sigma, \varepsilon_a^\sigma - \varepsilon_j^\sigma, E_{ex}, E_{em}, \Gamma_V, \Gamma_F)\times \sum_{\rho,\lambda=x,y,z}|\langle a_\sigma|m_\rho|i_\sigma\rangle|^2|\langle i_\sigma|m_\lambda|j_\sigma\rangle|^2 \tag{21}$$

3.5. Computational Details. All calculations were performed with the *ORCA* suite of quantum chemistry programs.[42] Scalar relativistic effects were treated explicity by employing second-order DKH[29−33] corrections. The BP86[43,44] and B3LYP[44−46] functionals were used together with Grimme's dispersion correction[47,48] for geometries/frequencies and electronic properties, respectively. The def2-TZVP basis set of Weigend et al. was used for all of the atoms in combination with the matching Coulomb fitting basis for the resolution of identity[49,50] (RI, in BP86 calculations). Quasi-restricted orbitals[51] were used for the DFT/ROCIS calculations. For these calculations, the B3LYP functional was employed together with the def2-TZVP(-f) basis sets. The necessary excitation space was constructed by using two donor and one acceptor orbital spaces. The first donor space involves the Mn 1s core orbital, while the second includes all of the relevant ligand 2s and 2p orbitals. Accordingly, the acceptor space is constructed by using all virtual orbitals necessary to describe the preedge and the onset of the rising edge. The configuration interaction space is constructed by $S' = S$ and $S' = S + 1$ excited CSFs. All calculated spectra include the SOC interaction.

The corresponding files for generating plots of the calculated RIXS planes, as well as the absorption or resonant emission profiles, were produced with the Orca_mapspc utility. Orca_mapspc is an integrated spectroscopic tool included in the *ORCA* suite of programs that is used to generate actual spectral envelopes from calculated transition energies and intensities. All calculated spectra were energy-shifted to match the energy position of the preedge and Kβ'' features for the corresponding XAS, non-resonant XES, and RXES spectra (137 and 170 eV for B3LYP/ROCIS and the BP86 one-electron approach, respectively). In addition, for XAS, XES, and RXES features, a Gaussian broadening of 1 eV was applied.

4. RESULTS AND ANALYSIS

Below, we will briefly recapitulate the experimental RIXS data for $(PPh_4)_2$ $[Mn(CN)_4N]$ in order to emphasize that the interpretation of these data requires a more elaborate approach than that required for either standard XAS or XES spectra. In order to approach this analysis systematically, we first describe the electronic structure of this complex. Given this information, the XAS and XES will be discussed before entering the more elaborate interpretation of the RIXS data.

4.1. Experimental RIXS Data. Figure 1A presents the previously reported experimental VtC XES RIXS plane for $(PPh_4)_2$ $[Mn(CN)_4N]$.[14] Parts B and C of Figures 1 present the XES and XAS cuts of the RIXS planes, respectively. As has been discussed previously, the vertical cuts at 6540 eV (blue line) and 6562 eV (green) correspond to the resonant VtC XES at the preedge and rising-edge XAS excitation energies, respectively. For reference, the non-resonant XES spectra are also shown (Figure 1B, black spectrum). For all of the VtC XES spectra (both resonant and non-resonant), one observes three features: Kβ'' at ∼6524 eV, K$\beta_{2,5}$(1) at 6531 eV, and K$\beta_{2,5}$(2)$''$ at ∼6535 eV. The largest differences in the XES spectra are

DOI: 10.1021/acs.inorgchem.7b01810
Inorg. Chem. 2017, 56, 11819−11836

observed upon resonant excitation into the preedge. Here two sharp well-resolved features are observed in the $K\beta_{2,5}$ region. Upon an increase in the excitation energy to ~6562 eV, the resonant XES spectrum becomes very similar to the non-resonant XES spectrum, with two broad features observed in the $K\beta_{2,5}$ region, appearing at somewhat higher energy. Moreover, for both XES and RXES spectra observed at 6521 and 6562 eV, the separations of the $K\beta_{2,5}(1)$ and $K\beta_{2,5}(2)$ features are similar and amount to about 4 eV. The horizontal cuts in Figure 1A correspond to XAS spectra detected at a constant emission energy. The individual XAS cuts at emission energies of 6543 eV ($K\beta''$), 6531 eV [$K\beta_{2,5}(1)$], and 6535 eV [$K\beta_{2,5}(2)$], together with the standard total fluorescence yield XAS spectrum, are shown in Figure 1C. Detection of XAS spectra from the $K\beta''$ emission feature results in a slight deenhancement of the preedge intensity relative to the total edge jump by a factor of ~2. On the other hand, detection of XAS from the $K\beta_{2,5}$ emission feature results in an enhancement in the detected preedge intensity relative to the edge jump by a factor of ~2.

In summary, very large intensity modulations are observed along both the absorption and emission axes, depending on the which transition one excites to or which transition one detects from. This means that there is a wealth of information to be obtained by analyzing these dramatic intensity variations in detail. However, as is shown herein, in order to interpret these spectra, a sophisticated theoretical approach is required that takes into account state polarization, interference between the intermediate states, and multiplet effects.

4.2. Electronic Structure and Geometric Properties. Figure 2 depicts the $[Mn^{V}N(CN)_4]^{2-}$ complex under study,

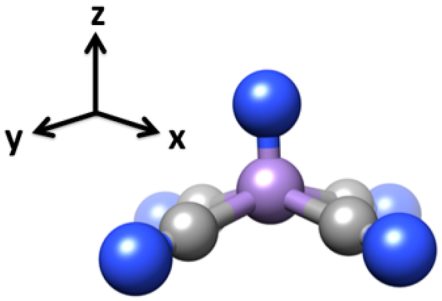

Figure 2. Molecular structure of the $[Mn^{V}N(CN)_4]^{2-}$ complex, together with the coordinate axis system. Color code: carbon, gray; nitrogen: blue; manganese, violet.

which contains Mn^{V} d^2 in a C_{4v}-symmetric coordination environment. The relevant ground-state core−valence electron configuration of $[Mn^{V}N(CN)_4]^{2-}$ dominating the XAS, XES, and RXES processes involves the $1a_1^2 2a_1^2 3a_1^2 4a_1^2\{...\}$-$6a_1^0 6e^0 2b_2^0 7a_1^0 7e^0\{...\}8a_1^0 8e^0$... MOs shown in Figures 3, 4, and S1 and S2.

Furthermore, the Mn K-edge XAS process involves excitations from the Mn $1s^2$ occupied core orbitals ($1a_1^2$) to the unoccupied manganese orbitals. Excitations to these orbitals cover the entire preedge and edge spectral area with singlet and triplet states. Because, however, there is no metal core−shell SOC and the ligand core−shell and valence d-shell SOC interactions are expected to be small, only the singlet states will predominately contribute to the K-edge XAS spectrum. Hence, in contrast to metal L- and M-edge XAS spectroscopies, the coupling of singlet and triplet states through SOC interactions will be small. Nevertheless, in an effort to keep our discussion as general as possible, we have included SOC effects in our calculations, and their effects in the calculated XAS and XES spectra will be discussed below.

Using group theoretical considerations, the XAS spectrum of $[Mn^{V}N(CN)_4]^{2-}$ is primarily dominated by states of $^{1,3}A_1$ and $^{1,3}E$ symmetries. As is shown in Figure 3, the valence states involve the $6a_1$ (Mn $3d_{z^2}$ and N $2p_z$), 6e (Mn $3d_{xy,yz}$ and N $2p_{x,y}$), and $7a_1$ (Mn 4s) MOs. In addition, the respective metal-to-ligand charge-transfer (MLCT) states involve the 7e (CN σ^*), $8a_1$ (N $2p_z$ and CN σ^*), and 8e (N $2p_{x,y}$ and CN σ^*) orbitals.

Non-resonant VtC XES involves states that are dominated by inner orbital electron decay in order to fill the 1s core hole. According to group theoretical considerations and assuming C_{4v} local coordination symmetry, this process again involves states of $^{1,3}E$ and $^{1,3}A_1$ symmetries, as shown in Figures 4 and S1. Furthermore, the VtC RXES event involves inner orbital electron decay upon core-electron excitation to valence orbitals. Apparently, such a process induces a much more complex multiplet structure compared than what is observed in standard XAS or VtC XES experiments. For example, coupling between the intermediate and final states of $^{1,3}E$ symmetry will result in $^{1,3}E_{intermediate} \otimes {}^{1,3}E_{final} = {}^{1,3}A_1 + {}^{1,3}A + {}^{1,3}B_1 + {}^{1,3}B_1$ states. A list of all relevant processes in the case of $[Mn^{V}N(CN)_4]^{2-}$ is provided in Figures 4 and S1. In particular, upon $1a_1^1 \rightarrow 6a_1^1$ core-to-valence excitations, the accompanying valence-to-core electron decays are

$$1a_1^1 2a_1^2 3a_1^2 4a_1^2 5a_1^2\{...\}6a_1^1 \rightarrow 1a_1^2 2a_1^2 3a_1^2 4a_1^2 5a_1^1\{...\}6a_1^1$$

$$1a_1^2 2a_1^2 4a_1^2 4a_1^1 5a_1^2\{...\}6a_1^1$$

$$1a_1^2 2a_1^2 3a_1^1 4a_1^2 5a_1^2\{...\}6a_1^1$$

$$1a_1^2 2a_1^1 3a_1^2 4a_1^2 5a_1^2\{...\}6a_1^1$$

This results in a complicated series of final state multiplets that is composed of contributions from all interfering intermediate states as described in eq 9. It should be noted that the core excited intermediate states of A and E symmetries will provide access to the final states with A and E symmetries, respectively. In fact, by just accounting for the contributions of the lowest-lying $1a_1^1 \rightarrow 6a_1^1$ excitations, the final-state multiplets involve the $^{1,3}A_1$, $^{1,3}A_1$, $^{1,3}A_1$, and $^{1,3}A_1$ nonrelativistic final states, which may further couple through SOC. This will result in 16 relativistic electronic states because each triplet state involves the three magnetic sublevels $M_s = -1, 0, 1$. Clearly, the complexity of the final-state-multiplet manifold grows rapidly with the number of accessible intermediate states. In a further step, the resonant emission process can be grouped according to the s- or p-ligand character of the inner decaying orbitals. Furthermore, as indicated in Figures 3, 4, and S1, inner orbitals with predominant p-ligand character reflect ideally the σ and π interactions of the involved coordinating atoms, while inner orbitals with predominant s-ligand character participate solely in σ interactions. Hence, in the case of the $[Mn^{V}N(CN)_4]^{2-}$ complex, at least three main features are expected in the VtC RXES spectrum, accounting for the $K\beta_{2,5}(1)$, $K\beta_{2,5}(2)$, and $K\beta''$ lines, respectively. However, as is shown in Figures 4 and S1, already within the particle−hole picture, there are several emission possibilities that may result in complicated XES and RXES spectral envelopes.

DOI: 10.1021/acs.inorgchem.7b01810
Inorg. Chem. 2017, 56, 11819−11836

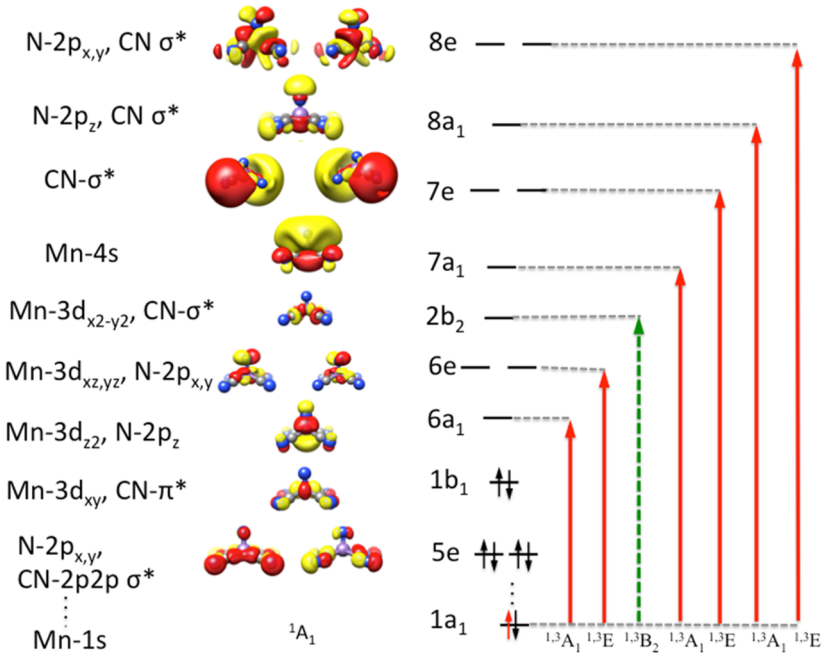

Figure 3. $[Mn^{V}N(CN)_4]^{2-}$ MOs and term symbols arising from single-electron-core excitations assuming C_{4v} symmetry. The long red arrows indicate dipole-allowed excitations, while the green dashed arrow indicates a dipole-forbidden excitation. The core-excited electron is indicated by the small red arrow. The indicated orbital occupation number refers to the $^1A_1$ ground state.

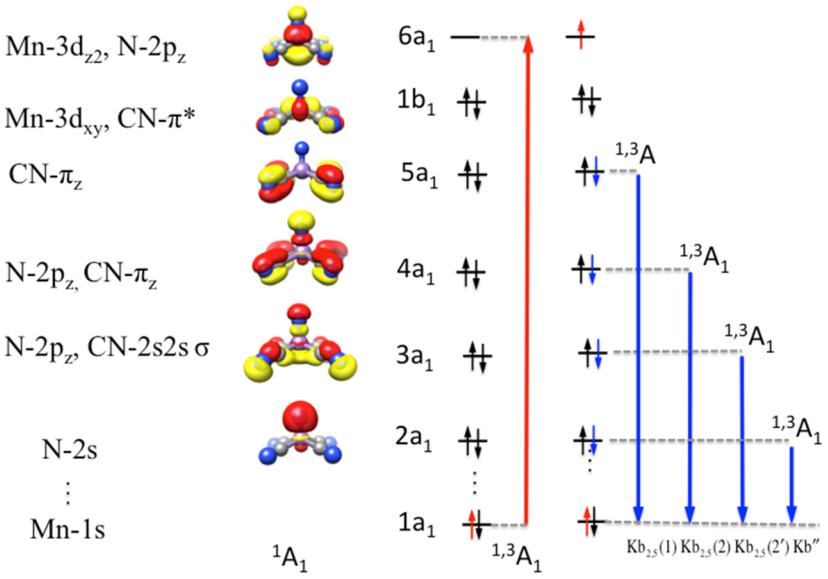

Figure 4. Example of a z-polarized RXES pathway within the direct process scheme. $[Mn^{V}N(CN)_4]^{2-}$ MOs and term symbols arising from single-electron-core excitations assuming C_{4v} symmetry (long red arrows). The core-excited electrons, as well as the resonant decay electrons, are indicated by the small blue and red arrows, respectively. The long blue arrows and corresponding term symbols reflect resonant emission processes. The indicated orbital occupation number refers to the $^1A_1$ ground state.

4.3. XAS. *4.3.1. Nonrelativistic Treatment.* Prior to the analysis of the VtC RXES spectra, it is usuful to analyze the nature of the dominating features of the corresponding XAS spectra. For this purpose, the $[Mn^{V}N(CN)_4]^{2-}$ Mn K-edge XAS spectra were calculated at various levels of theory and compared against the experimental TFY XAS data. As shown in Figure 5, in a first approximation, particle−hole approaches are employed in terms of (1) a DFT one-electron approach utilizing the BP86 functional and (2) TD-DFT calculations with the BP86 and B3LYP functionals, respectively. In addition, wave-function-based calculations were performed at the B3LYP/ROCIS level. In order to facilitate comparisons between theory and experiment, we have chosen to normalize the preedge energy regions of the experimental versus calculated XAS spectra. In this way, it is possible to monitor the intensity enhancements and deenhancements in the preedge and rising-edge regions under resonant conditions. In general, the integrated area of the experimental edge data is much larger than the calculated ones. Hence, in all calculations, the relative intensity of the edge features located at 6557 eV appears to be overestimated. This is partly due to the fact that the edge region is affected by extra shakeup/down excitation

DOI: 10.1021/acs.inorgchem.7b01810
Inorg. Chem. 2017, 56, 11819−11836

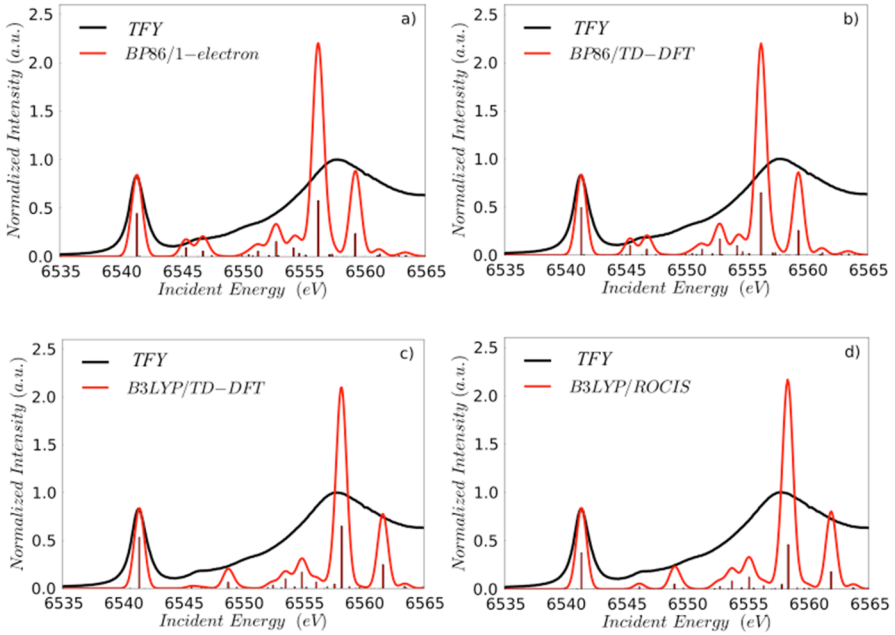

Figure 5. Black: Experimental Mn K-edge TFY spectra. Red: Calculated XAS spectra at BP86/one-electron (a), BP86/TD-DFT (b), B3LYP/TD-DFT (c), and B3LYP/ROCIS (d) levels of theory. Stick lines correspond to the contributing states. All calculated spectra were energy-shifted 137−170 eV to match the preedge feature. A constant line-shape broadening of 1 eV was applied.

processes or multiple scattering events that are not captured by the theories applied here. In addition, the different nature of the involved excitations in these regions might result in different line-broadening mechanisms. This would justify the use of different line broadenings for the preedge and edge regions; however, as described in the Computational Details, we decided to use a constant line-shape broadening in order to describe the important electronic effects in a more transparent way. Further inspection of the calculated versus experimental spectra reveals that the particle−hole approaches employing the BP86 functional underestimate the relative splitting between the preedge and edge features (Figure 5, top panels). On the other hand, when the B3LYP functional is employed, both TD-DFT and DFT/ROCIS spectra of similar quality are obtained, in which the splitting of the preedge and edge features is nicely reproduced (Figure 5, bottom panels). In fact, apart from the preedge and main-edge features located at 6541 and 6557 eV, the characteristic double-featured shoulder centered at 6547 eV is also nicely reproduced.

4.3.2. Effects of SOC. In the next step, we perform DFT/ROCIS calculations by including states of singlet ($2S + 1 = 1$) and triplet ($2S + 1 = 3$) spin multiplicities in the configuration interaction treatment in order to examine the effect of SOC in the calculated Mn K-edge XAS spectrum. Further insight into these calculated features can be obtained by tracing the nonrelativistic character of the relativistically corrected states in terms of singlet and triplet spin multiplicities. In this way, it is possible to regenerate the SOC-corrected spectrum, together with the subspectra, that involve relativistic states with parent singlet or triplet nonrelativistic character. A similar analysis has proven to be successful in the description of the intensity mechanisms operative in the metal L-edge and O K-edge XAS spectra in various transition-metal compounds, as well as in solid networks.[28,52] The nature of the calculated features is discussed in terms of states contributing with singlet ($2S + 1 = 1$) and triplet ($2S + 1 = 3$) spin multiplicities that are mixing through SOC and result in the relativistically corrected calculated many-particle spectra. As can be seen in Figure 6, the main-edge region of the XAS spectrum contains significant

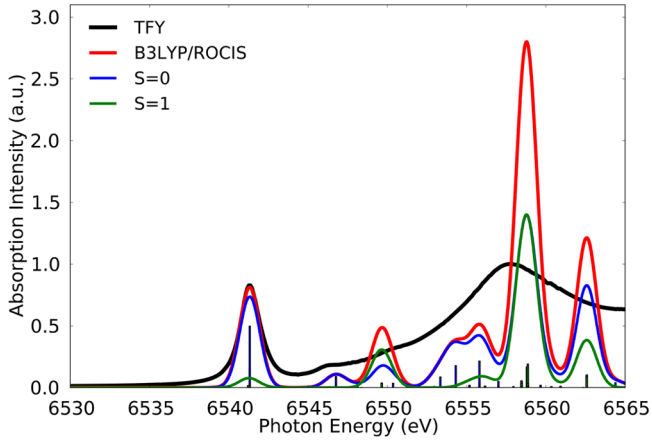

Figure 6. Black: Experimental Mn K-edge TFY spectra. Red: SOC-corrected B3LYP/ROCIS-calculated spectra. Stick lines correspond to the contributing relativistically corrected states. Blue and green lines correspond to the individual subspectra formed by the relativistic states with parent nonrelativistic multiplicities $2S + 1 = 1$ and $2S + 1 = 3$, respectively. All calculated spectra were energy-shifted 137 eV to match the preedge feature. A constant line-shape broadening of 1 eV was applied.

contributions from triplet states. Because, however, SOC arises mainly from the valence d shell, as expected, the shapes of the nonrelativistic and relativistically corrected spectra (Figures 5 and 6) remain practically unaffected, reflecting the very small exchange integrals between the core and valence orbitals that split these states. However, the intensity of some features is affected, and these are invariably those for which the triplet character is high (~35%).

4.4. XES. The performance of the DFT one-electron approach, as well as the DFT/ROCIS method, has been

DOI: 10.1021/acs.inorgchem.7b01810
Inorg. Chem. 2017, 56, 11819−11836

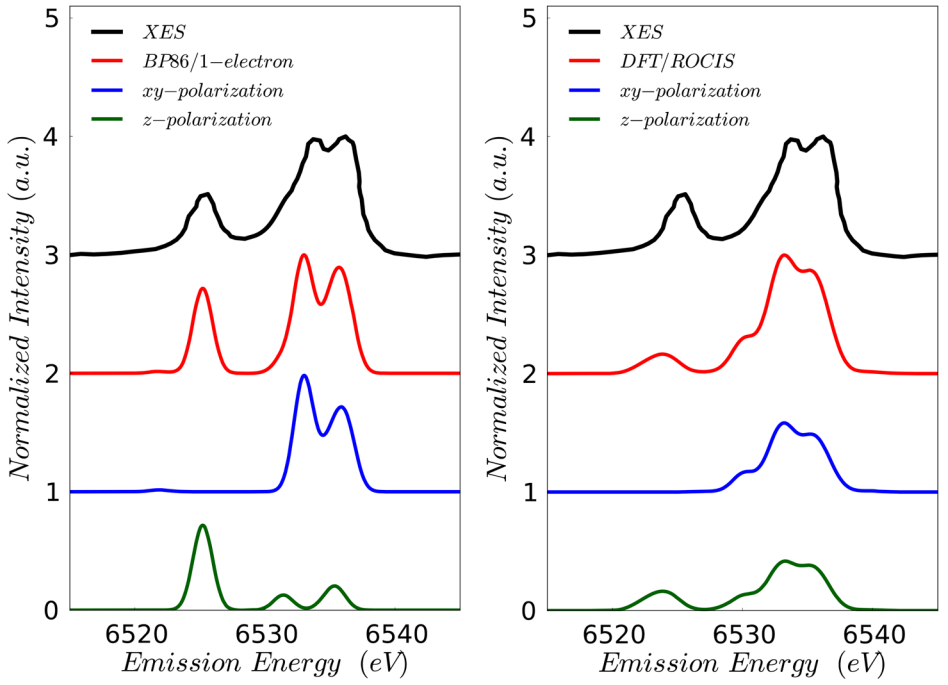

Figure 7. Black: Experimental non-resonant XES spectra. Red: Calculated spectra involving the one-electron approach as well as DFT/ROCIS with SOC corrections. Blue and green spectra indicate *xy*- and *z*-polarized spectra, respectively. All calculated spectra were energy-shifted 137−170 eV. A constant line-shape broadening of 1 eV was applied.

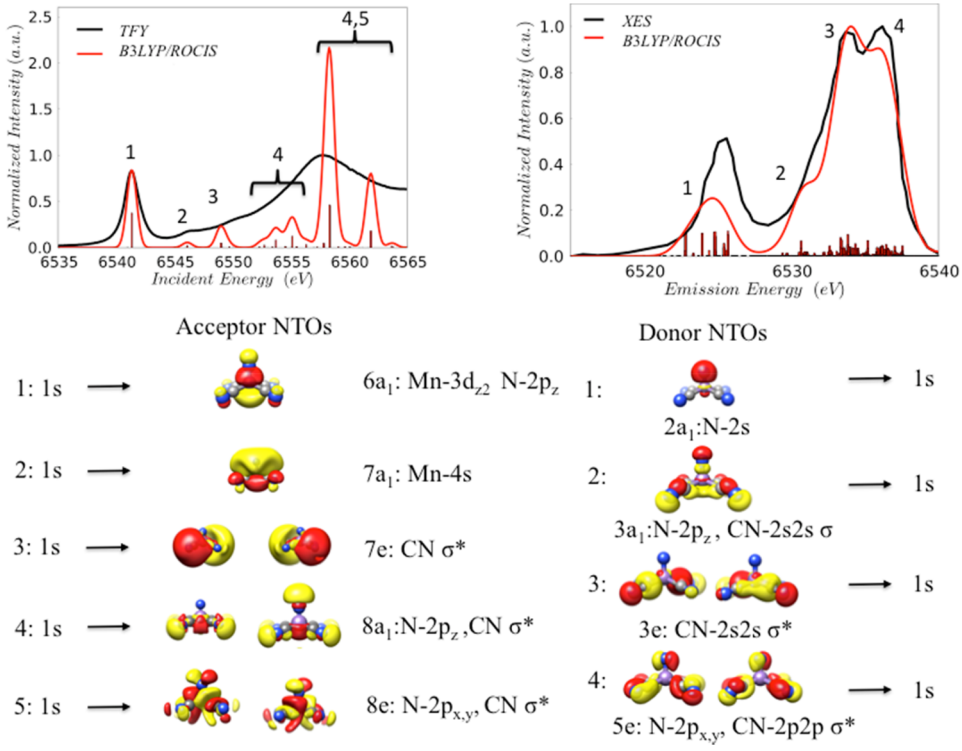

Figure 8. Top: Experimental (black) versus DFT/ROCIS-calculated (red) XAS and VtC XES spectra. Bottom: Natural transition orbital analysis of the main features dominating the corresponding XAS and VtC XES spectra.

further evaluated for calculation of the non-resonant VtC XES spectrum of the $[Mn^{V}N(CN)_4]^{2-}$ complex. As can be seen in Figure 7, the BP86 one-electron approach achieves good agreement with experiment and successfully reproduces the main experimental features located at 6524, 6531, and 6535 eV. However, agreement with the experimental spectrum is improved when the B3LYP/ROCIS method is employed because, in addition, an experimental shoulder observed at 6529 eV is clearly observed. In particular, the correct intensity distribution, as well as the number of the observed experimental features, is reproduced by the SOC-corrected B3LYP/ROCIS-calculated spectra.

DOI: 10.1021/acs.inorgchem.7b01810
Inorg. Chem. 2017, 56, 11819−11836

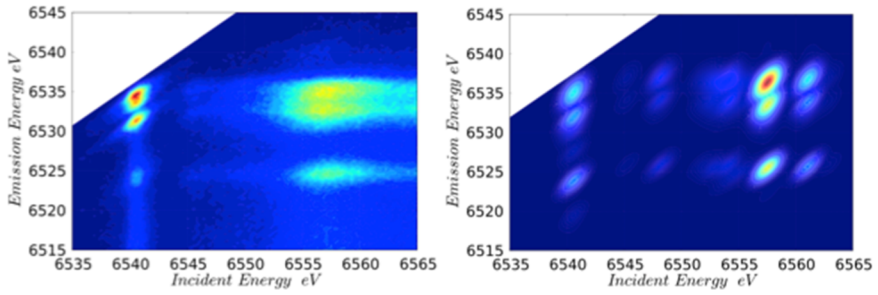

Figure 9. Experimental versus B3LYP/ROCIS-calculated VtC RXES planes by employing the direct intensity map (eqs 13 and 21). All calculated planes are energy-shifted 137 eV along the incident axis, while a constant line broadening of 1 eV is applied along both axes.

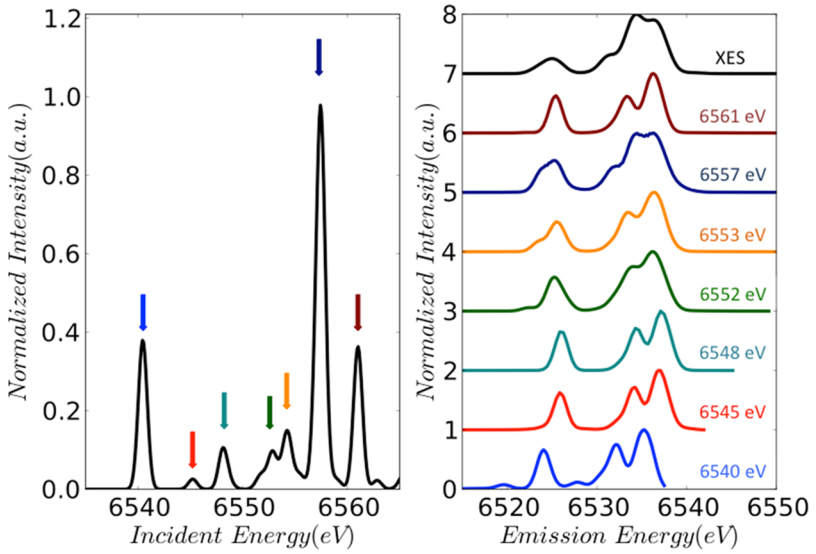

Figure 10. Calculated spectra within the DFT/ROCIS method. The left panel shows calculated XAS spectra. Arrows indicate incident energies at which the respective resonant XES spectra (right panel) were generated. All calculated spectra were energy-shifted 137 eV. A constant line-shape broadening of 1 eV was applied. The trace labeled XES corresponds to the calculated non-resonant XES spectrum.

Furthermore, analysis of the polarized subspectra indicates that the Kβ'' band located at ~6524 eV is *z*-polarized, while the K$\beta_{2,5}$ bands located at 6529, 6531, and 6534 eV are both *z*- and *xy*-polarized, in agreement with the experimental observations of XES studies performed on a $[Rh(en)_3][MnN(CN)_5]H_2O$ single crystal.[53]

4.5. XAS and XES Analysis. In this section, the DFT/ROCIS-calculated XAS and VtC XES spectra are analyzed by using the natural transition orbitals. As can be seen in Figure 8, these spectra are dominated by states that can be arranged in groups of five and four transitions, respectively. In particular, the preedge region (6540−6545 eV) of the XAS spectrum is dominated by the valence excitations 1s → $6a_1(3d_{z^2})$, 1s → $6e(3d_{xy/yz})$, and 1s → $7a_1(4s)$ (bands 1 and 2, respectively; Figure 8). On the other hand, the corresponding rising- and main-edge regions ranging between 6545 and 6565 eV (bands 3−5) are dominated by the following MLCT single-electron excitations: 1s → 7e (CN σ^*), $1s8a_1$ (N $2p_z$ and CN σ^*), and 1s8e (N $2p_{x,y}$ and CN σ^*) (Figure 8). Similarly, the experimental feature of the VtC XES spectrum located at 6524 eV (band 1) is dominated by N $2s2a_1$ → 1s electron decays. Moreover, the features located at 6529, 6532, and 6536 eV (bands 2−4) are dominated by (N $2p_z$, CN 2s2s σ)$3a_1$ → 1s, (CN 2s2s σ^*)3e → 1s, and (N $2p_{xy}$, CN 2p2p σ)5e → 1s electron decays, respectively (Figures 4 and S1). These results further suggest that DFT/ROCIS can successfully support the experimental polarization trends in the Kβ'' and K$\beta_{2,5}$ regions. Additional insight can be obtained by analyzing the metal dp and ligand p character of the XES donor MOs. These results are presented in Tables S1 and S2. As can be seen, the observed transition dipole intensities (Figure 8, top right) map nicely with the amount of metal p character in the XES donor MOs, which amounts to 8.2%, 1.7%, 9.5%, and 4.9% for transitions 1−4, respectively.

4.6. Calculated RIXS Planes. *4.6.1. Overall Spectral Trends.* Following the protocol described in the theoretical and computational sections, the corresponding VtC RXES planes are generated by using a one-electron DFT approach, as well as the DFT/ROCIS method, according to eqs 21 and 13−15, respectively. It is important to recall that, from these equations, the major contributions to the RIXS intensity can be written as $|\alpha|^2 \propto m_{FV}m_{VI}$, where m_{FV} is the transition dipole vector between the final and intermediate states and m_{VI} is the respective transition dipole vector between the intermediate and initial states. It follows that the intensity will be zero if the two transition dipoles are orthogonal to each other and at a maximum if they are collinear. The system under investigation here has axial symmetry, and it was shown in the previous sections how this symmetry is reflected by the polarization dependence of the XAS and XES spectra. Hence, it is sensible to analyze the RIXS data in terms of *xy*- and *z*-polarized pathways, respectively.

DOI: 10.1021/acs.inorgchem.7b01810
Inorg. Chem. 2017, 56, 11819−11836

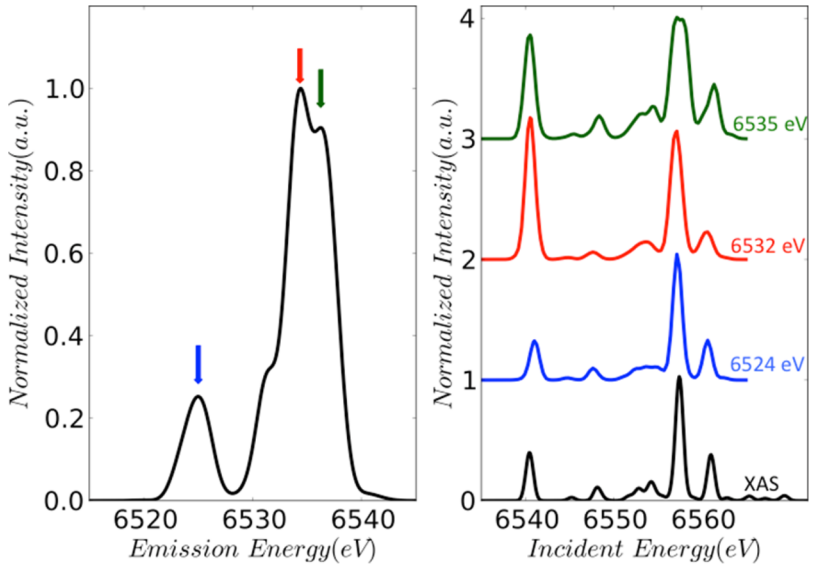

Figure 11. Calculated spectra within the DFT/ROCIS method. The left panel shows the calculated non-resonant XES spectrum. Arrows indicate emission energies at which the respective HERFD XAS spectra were generated, as shown in the right panel. All calculated spectra were energy-shifted 137 eV. A constant line-shape broadening of 1 eV was applied. The trace labeled XAS corresponds to the calculated standard XAS spectrum.

The calculated RIXS planes are shown in Figures 9 and S3. A comparison of the experimental versus calculated planes shows that qualitatively both approaches agree well with the experiment. In fact, along both incident energy and emission axes, the main experimental features are nicely reproduced. For example, along the emission axis, the expected three signals corresponding to the Kβ'' and K$\beta_{2,5}$(1,2) features are observed at 6524, 6532, and 6536 eV. In addition, along the incident axis, the observed signals reflect the respective XAS patterns. As discussed for the respective XAS spectra, once again the relative intensity of the main-edge region with respect to the preedge region is overestimated with both approaches. However, only the DFT/ROCIS method is able to reproduce the correct relative energy position of these regions.

4.6.2. Cuts along Constant Incident/Emission Energies. In an effort to obtain further insight into the calculated features in terms of multiplet structure and interference effects, we analyze below the XAS and XES spectra under resonance conditions generated as cuts along constant emission and constant incident energy, respectively, for both the one-electron approach (Figures S4 and S5) and the DFT/ROCIS method (Figures 10 and 11). As has been discussed previously, the one-electron approach has been proven to be unable to describe the correct intensity distribution in a series of manganese complexes including the one studied here.[14] In fact, as shown in Figures S4 and S5, both XAS and XES spectra calculated at constant emission and incident energies either are very similar to the respective XAS and XES spectra calculated at non-resonant conditions shown with black lines or, in the case of XES spectra, show only limited intensity distribution at high energies. This is in sharp contrast to what is observed experimentally, as demonstrated in Figure 1.

The situation changes rapidly when the DFT/ROCIS method is employed to calculate the relevant spectra (Figures 10 and 11). In the case of the calculated XES spectra generated at constant incident, it is seen that excitations at the preedge region (6540 eV) result primarily in three well-separated spectral features located at 6524, 6532, and 6536 eV. Excitations in the main-edge region (6557 eV) result in a XES spectrum, which closely resembles the non-resonant XES spectrum with four spectral features located at 6525, 6531, 6533, and 6535 eV. These trends are in very good agreement with experiment. Similarly, the calculated XAS spectra obtained at constant emission energies in the K$\beta_{2,5}$(1,2) region (6535 and 6532 eV) result in XAS preedge intensities that is ∼1.5 and 2 times higher than that calculated for a standard Mn K-edge XAS spectrum. Similarly, the calculations also predict that the XAS spectrum generated by monitoring the Kβ'' emission energy (6524 eV) should have a reduced preedge intensity. This is again in complete accordance with experimental observations. Furthermore, upon inspection of Figure 10, it becomes evident that the generated RXES spectra at constant incident energies display peaks that apparently shift in energy. This indicates that a different set of final states dominate the spectra at different incident energies. In the following sections, the VtC intensity mechanism will be analyzed in detail.

4.6.3. Insights into the Nature of the Final States Dominating the RXES Spectra. In keeping with the discussion in section 4.6.1, we first discuss the magnitudes of the transition moments of the major absorptive and emissive processes along the *z*- and *xy*-polarized pathways presented in Figures 4 and S1. These results are summarized in Schemes 2a,b. Inspection of these values shows that the largest contributions to the RIXS intensity arise if both transitions are collinear and have large individual transition dipoles. Hence, a weak absorption feature will be less likely than an intense emission feature and vice versa.

Along the *z*-polarized pathway, the preedge XAS feature [dominated by the 1s → 6a$_1$ (1s → 3d$_{z^2}$) transition] has a larger associated transition moment (by 1−2 orders of magnitude) than the 1s → 7a$_1$ (1s → 4s) and 1s → 8a$_1$ (1s → N 2p$_z$ and CN σ^*) transitions, which are associated with the rising edge (Scheme 2a). This pattern is reversed for the *xy*-polarized pathways (Scheme 2b). At the non-resonant XES limit, the intensities of the primary K$\beta_{2,5}$ features carry larger transition moments with respect to the Kβ'' ones, while the secondary K$\beta_{2,5}$(2′) features are 1−2 orders of magnitude lower. These trends to a large extent are also reflected in the metal p and d

DOI: 10.1021/acs.inorgchem.7b01810
Inorg. Chem. 2017, 56, 11819−11836

Scheme 2. Major Contributions of the Dipole Transition Moments for the Absorptive ($10^6 D_{IV}^2$, Red Arrows) and Non-resonant Emissive ($10^3 D_{VF}^2$, Blue Arrows) Processes between the Initial, Intermediate, and Final (*I*, *V*, and *F*) States along (a) *z*- and (b) *xy*-Polarized Pathways[a]

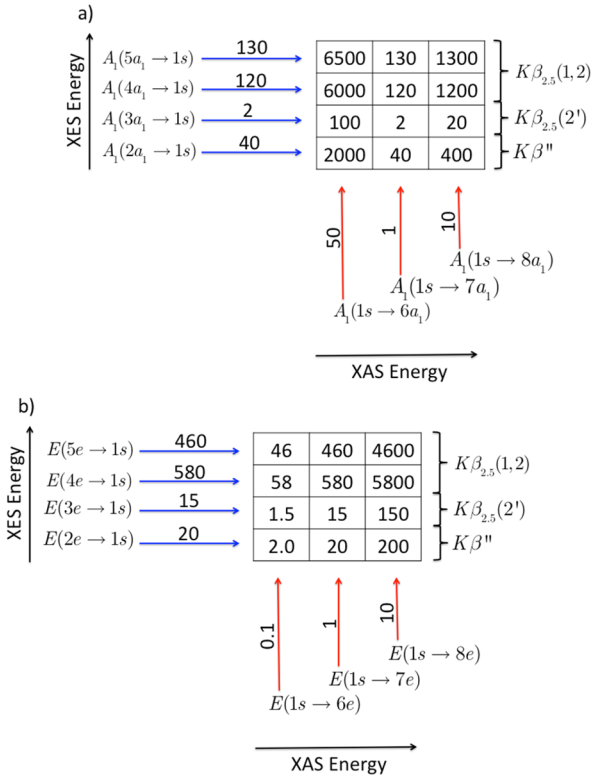

[a]The transition dipole product matrix for the direct RXES process ($10^9 D_{IV}^2 D_{VF}^2$; eq 9) in atomic units as well as the dominant single-electron excitation and decays is also provided.

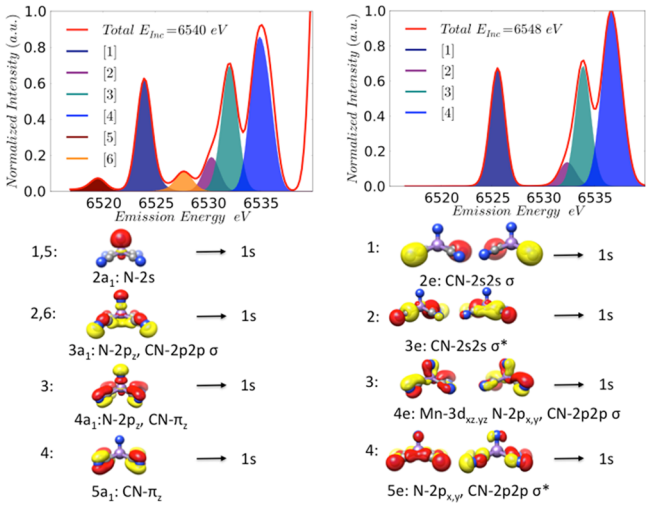

Figure 12. Top: B3LYP/ROCIS-calculated RXES spectra at 6540 and 6548 eV incident energy spectra. Filled lines indicate contributions from the final states per given intermediate state. Bottom: Natural transition orbital analysis of the main features dominating the corresponding RXES spectra. All calculated spectra were energy-shifted 137 eV. A constant line-shape broadening of 1 eV was applied.

character of the respective XAS acceptor and XES donor MOs, as summarized in Table S1. Similar observations can be drawn along the *xy*-polarized pathways by inspection of Scheme 2b and Table S2.

In a further step, insight into the RXES intensities can be obtained by coupling the XES and XAS transition moments assuming the direct VtC RXES process (eq 10). As reflected in the values of the products of the $D_{IV}^2 D_{VF}^2$ transition dipole moments shown in Scheme 2a,b, the RXES spectra generated at the preedge XAS features will be solely *z*-polarized, while the RXES spectra generated at the rising- and main-edge RXES spectra will be both *z*- and *xy*-polarized.

Among the spectra presented in Figure 10, we choose to analyze in detail two characteristic examples of the RXES spectra generated at incident energies of 6540 and 6548 eV, respectively. At these energies, the XAS process involves states that are dominated by the *z*-polarized 1s → $6a_1$ (1s → $3d_{z^2}$) and the *xy*-polarized equatorial CNs [1s → 7e (CN σ^*)] single-electron excitations, respectively. The resultant VtC RXES spectra are visualized in Figure 12, together with the respective donor natural transition orbitals dominating the final states. Analysis of the dominating natural transition orbitals shows that the two spectra are shifted in energy with respect to each other owing to the different nature of the involved final states. In particular, the RXES spectrum generated at 6540 eV excitation energy is dominated by states showing mainly a *z*-polarized single-electron decay pattern, while the RXES spectrum generated at 6548 eV contains contributions from states showing mainly a *xy*-polarized single-electron decay pattern. This is in agreement with the fact that the states involved in the absorption and emission processes must have nonorthogonal transition dipole moments in order to have nonzero RXES intensity.

Moreover, the VtC RXES spectrum at 6540 eV shows two additional bands, [5] and [6], located at 6519 and 6527 eV. Analysis of the involved natural transition orbitals indicates that bands [1] and [5] as well as bands [2] and [6] contain information on final states with similar single-electron decay patterns. However, further analysis shows that the above pairs of bands differ by the single-electron excitation pattern of their intermediate states. In fact, as can be seen in Figure S2, the bands located at 6519 and 6527 eV are dominated by the higher-energy intermediate states with single-electron excitation character $1a_1 \rightarrow 6'a_1$. Hence, because all of the above intermediate states are within the vicinity of the resonant excitation, they are all contributing features to the RXES spectra.

4.6.4. Insights into the Nature of the Final States Dominating the XAS Spectra. In a second step of the analysis, we discuss the XAS-detected spectra at various constant emission energies. Similar to the RXES intensity analysis presented above, we first inspect the transition dipole moment products of the direct VtC process given in Scheme 2a,b. As can be seen, the XAS spectra generated at Kβ'' emission feature has preedge and main-edge features that are mainly *z*- and *xy*-polarized, respectively. This is also reflected on the XAS spectra generated at the primary K$\beta_{2,5}$(1,2) emission energies, however at much higher intensities because the respective parent XAS and non-resonant XES processes carry the largest magnitude of the transition dipole moments (Scheme 2a,b). This is consistent with the fact that the involved donor and acceptor XAS and XES MOs contain significant metal p character (Tables S1 and S2). Along both pathways, as a result, the

DOI: 10.1021/acs.inorgchem.7b01810
Inorg. Chem. 2017, 56, 11819−11836

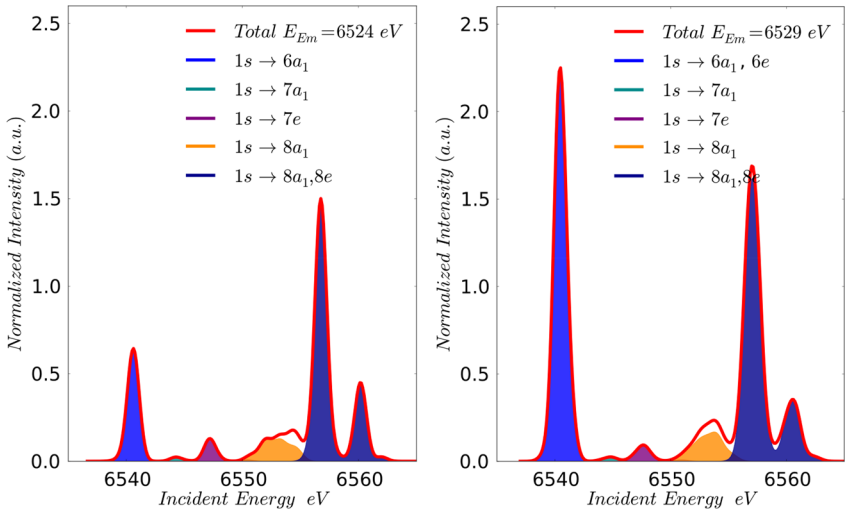

Figure 13. DFT/ROCIS-calculated (red line) XAS spectra generated at 6524 eV (left) and 6529 eV (right). Filled lines indicate contributions from the various intermediate states in terms of single-electron contributions. A constant shift of 137 eV was applied to the calculated incident axis.

preedge and main-edge features are strongly polarized, while their relative intensities may be reversed.

In a manner similar to analysis of the VtC RXES spectra, a quantitative description of the calculated HERFD XAS spectra can also be obtained by analyzing the individual contributions of the intermediate states for a given final state. As shown in Figure 13, the detection of XAS at K$\beta_{2,5}$ emission energies (6529 and 6532 eV) involves intermediate states that are dominated by valence 1s → 6a$_1$ (1s → 3d$_{z^2}$) and 1s → 6e (1s → 3d$_{xy/yz}$) excitations. This is in contrast to the excitation pattern observed for the TFY XAS and the XAS spectra detected at Kβ'' emission energy (6524 eV). In these latter cases, the preedge feature is solely dominated by 1s → 6a$_1$ (1s → 3d$_{z^2}$) single-electron excitations. In particular, analysis shows that the major contribution arises from the coupling of the *z*-polarized intermediate states [dominated by 1s → 6a$_1$ (1s → 3d$_{z^2}$) single-electron excitations] with the final states of K$\beta_{2,5}$(1) [6529 eV; dominated by the *z*-polarized 5a$_1$ → 1s (CN π_z and N 2p$_z$ → 1s) electron decays]. This coupling provides significant intensity enhancement to the preedge XAS feature. Further analysis shows that coupling of the *xy*-polarized intermediate states dominated by 1s → 6e (1s → 3d$_{xz/yz}$) single-electron excitations with the final states of K$\beta_{2,5}$(2) (6532 eV) that are dominated by the *xy*-polarized 4e → 1s (3d$_{xz/yz}$, CN 2p2p σ, and N 2p$_{x,y}$ → 1s) electron decays provides an alternative but weaker, intensity-enhancing mechanism for the preedge XAS feature.

4.6.5. Interference Effects of the Intermediate States in the RXES and XAS Spectra. In a final step of our analysis, we discuss the influence of the interference effects on the intensity mechanism. As eq 9 dictates, interference effects may arise during the resonance excitation process into the manifold of the intermediate states. The strength of the interference effects can be estimated by generating the direct, total, and interference planes according to eqs 13−15, as presented in Figure S3. It should be mentioned that no interference effects are observed in the preedge region of the XAS spectra generated at constant emission energies or when RXES spectra are generated by excitation into the preedge XAS region. On the other hand, positive and negative interference contributions to the intensity are observed in the main-edge region of the XAS spectra observed at constant emission energies and in the RXES spectra generated by excitation into the main-edge XAS region. In the RXES spectra, these effects contribute to about 10% of the total intensity, while in the case of the respective XAS spectra, these effects are rather negligible.

In an effort to understand the mechanisms of these contributions to the polarized VtC RXES intensity, we consider a model case that involves just two intermediate states $|V_1\rangle$ and $|V_2\rangle$. Hence, the nominator in eq 9 reads

$$\text{nom} = |\langle F|m_\rho|V_1\rangle|^2|\langle V_1|m_\lambda|I\rangle|^2 + |\langle F|m_\rho|V_2\rangle|^2|\langle V_2|m_\lambda|I\rangle|^2 \pm 2|\langle F|m_\rho|V_1\rangle\langle V_1|m_\lambda|I\rangle\langle F|m_\rho|V_2\rangle\langle V_2|m_\lambda|I\rangle| \quad (22)$$

In accordance with the discussion above, the direct VtC RXES process, described by the squared transition dipole products in eq 22 and schematically depicted in Figure 14 (cases 1 and 2), provides a state coupling mechanism between state pairs with nonorthogonal transition dipole moments. In addition, as indicated by the states that are marked in green, this process

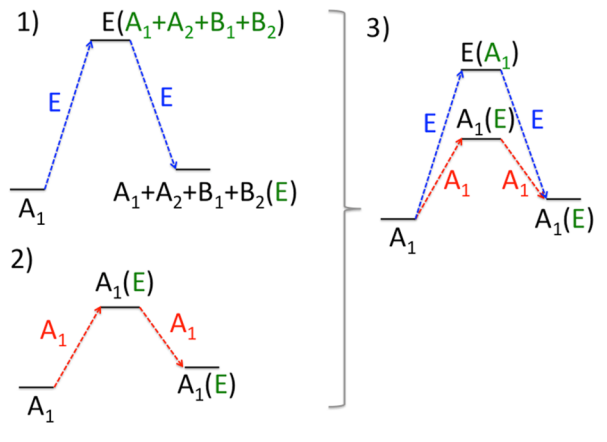

Figure 14. Possible state coupling channels along the direct VtC RXES process along the *z*- and *xy*-polarized pathways indicated with blue and red dotted arrows, respectively (cases 1 and 2). Case 3: Additional state coupling channels along the VtC RXES process, which become accessible via the total VtC RXES process. Nominally dipole-forbidden pathways along the conventional XAS and XES processes, which become accessible via the resonant state coupling mechanisms, are marked green.

DOI: 10.1021/acs.inorgchem.7b01810
Inorg. Chem. 2017, 56, 11819−11836

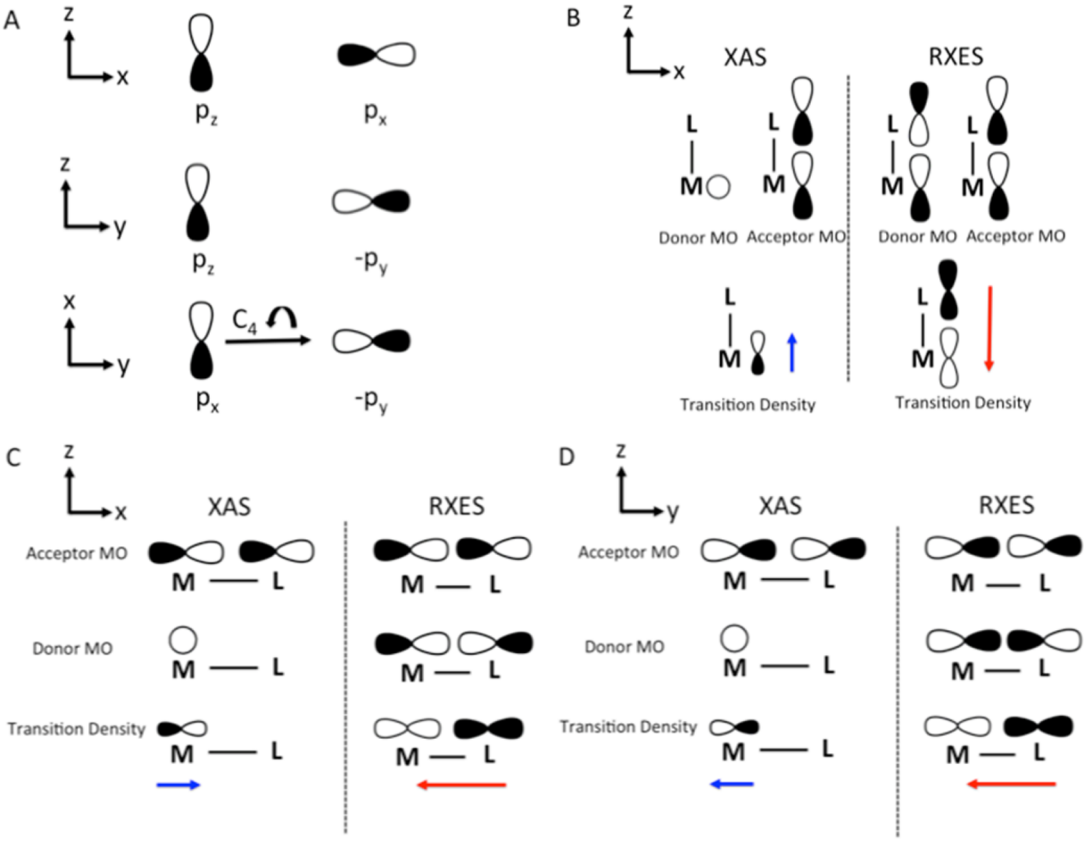

Figure 15. (A) Transformation of p orbitals under symmetry rotation about the 4-fold C_4 axis. Comparison of the electric-dipole-intensity mechanisms for VtC RXES along the (B) *z*, (C) *x*, and (D) *y* directions. Blue and red arrows indicate the transition dipole moment direction along the XAS and RXES dimensions, respectively.

gives the intensities to transitions that are symmetry-forbidden in standard single-photon experiments. It should be emphasized that, assuming ideal C_{4v} symmetry around the metal center, one can distinguish the excitation process between dipole-allowed and dipole-forbidden transitions, and these selection rules will not be broken by the interference process. However, because the coordination environment lowers the symmetry around the metal center to less than C_{4v}, nominally dipole-forbidden transitions might carry some intensity and these contributions may be "amplified" in the interference process. In this view, the interference contributions in eq 22 provide an additional intensity-enhancing mechanism in which the nominally dipole-forbidden emissive *z*- and *xy*-polarized pathways may gain intensity from the dipole-allowed absorptive *z*- and *xy*-polarized pathways through interference and vice versa. This is depicted in Figure 14 (case 3). For example, as can be seen, the dipole-allowed emissive *z*- and *xy*-polarized pathways $A_1 \xrightarrow{A_1} A_1$ and $E \xrightarrow{E} A_1$ from the dipole-allowed *xy*-polarized E and *z*-polarized A_1 intermediate states can gain or lose intensity via interference. Likewise, the respective nominally dipole-forbidden emissive *z*- and *xy*-polarized pathways $A_1 \xrightarrow{A_1} E$ and $E \xrightarrow{E} E$ may gain intensity from the dipole-allowed absorptive *z*- and *xy*-polarized pathways $A_1 \xrightarrow{A_1} A_1$ and $A_1 \xrightarrow{E} E$ through interference. Such phenomena have been observed in recent 1s2p RXES studies of small molecules, where it has been demonstrated that state interference effects are able to break the parity selection rules.[54,55]

As illustrated in Figure 15, the states involved in the XAS and RXES processes are dominated by single-electron excitations with significant metal p character. Similar to MLCT excitations,[56] the VtC RXES process describes a charge-transfer (CT) type of electron decay in which the transition density contains a dominant contribution proportional to the M−L distance because both the donor and acceptor MOs are shared between the metal and ligand, which introduces a large transition dipole moment along the M−L bond. It should be noted that this contribution describes the shift of the electron density from the ligand to the metal upon CT decay. Such a contribution is not present in the metal K-edge intensity, as the donor MO is completely localized on the metal. Furthermore, one can estimate the phase of the transition dipole moment for the combined process along the *z* and *xy* directions. This way of analyzing transition dipole properties has been proven to be instrumental in understanding the principles of the intensity mechanism in ligand K-edge XAS and the MLCT of the UV/vis spectra,[56] as well as predicting the sign of the *C* terms in magnetic circular dichroism spectroscopy.[57,58]

As can be seen in Figure 15A, in C_{4v} symmetry, the p orbitals under the rotation action about the 4-fold C_4 axis transform as $p_x \rightarrow p_y$, which is reflected in their relative phases. In the above orbital phase-symmetry-adapted convention along the *z*, *x*, and *y* directions, we further evaluate the phases of the M−L transition densities for the resonant absorptive (XAS) and emissive (RXES) processes, and we derive the directions of the respective transitions dipole moments graphically. As can be seen along the *z* direction (Figure 15B), the XAS and RXES transition dipole moments have opposite phases. On the other

DOI: 10.1021/acs.inorgchem.7b01810
Inorg. Chem. 2017, 56, 11819−11836

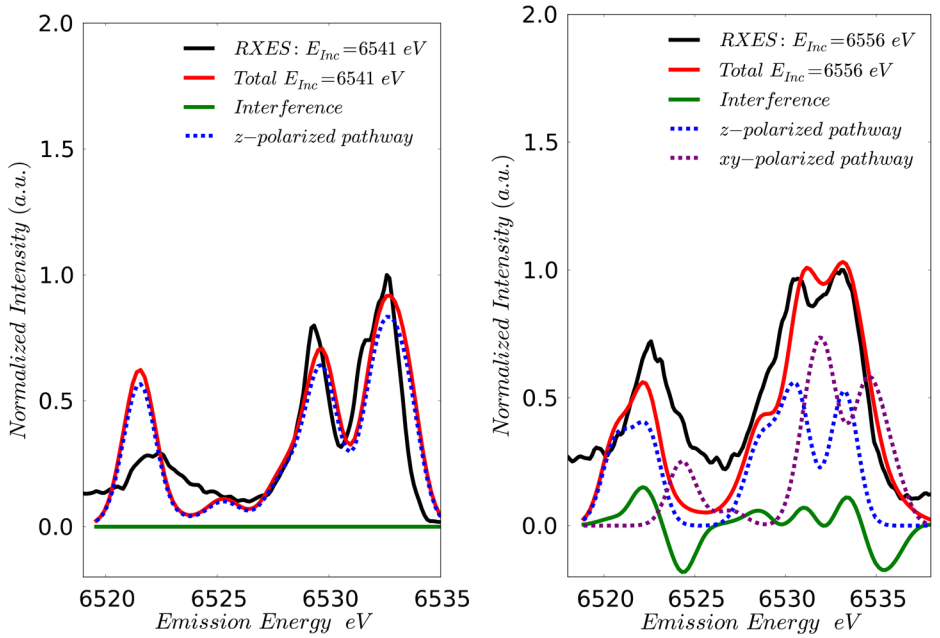

Figure 16. Experimental (black) versus DFT/ROCIS-calculated (red) RXES-detected spectra for $[Mn^{V}N(CN)_4]^{2-}$. The experimental spectra were taken at emission energies of 6541 eV (left) and 6556 eV (right). The green line indicates interference contributions to the total intensity, while the blue and purple dashed lines indicate contributions along the *z*- and *xy*-polarized pathways, respectively. All calculated spectra were energy-shifted 137 eV. A constant line-shape broadening of 1 eV was applied.

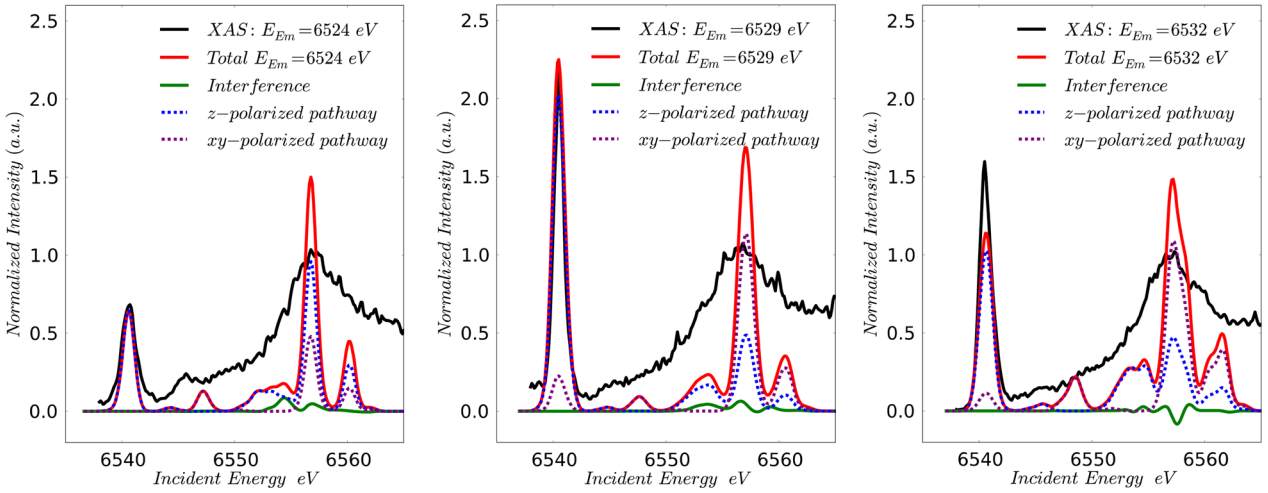

Figure 17. Experimental (black) versus DFT/ROCIS-calculated (red line) XAS spectra for $[Mn^{V}N(CN)_4]^{2-}$. The experimental spectra were taken at emission energies of 6524 eV (left), 6529 eV (middle), and 6532 eV (right). The green lines indicate interference contributions, while blue and purple dashed lines indicate contributions along the *z*- and *xy*-polarized pathways, respectively. A constant shift of 137 eV was applied to the calculated incident axis.

hand, along the *x* and *y* directions (Figure 15C,D), the respective transition dipole moments may have the same or opposite phases. Hence, we conclude that state coupling between *z*-polarized intermediate states will lead to destructive interference (nom < 0 in eq 22), while state coupling between *xy*-polarized intermediate states will lead to either constructive or destructive interference (nom > 0 or nom < 0 in eq 22). Clearly, interference effects are able to provide significant intensity modulations. In the next section, their influence to the intensity mechanism of the XAS and RXES spectra will be discussed in detail.

4.6.6. VtC RXES Intensity Mechanism. In this section, we will combine all of the above observations in order to summarize the insights obtained in the complex mechanism of the VtC RXES process. We recall that there are two general rules:

(1) In a direct VtC RXES process as described in eq 13, coupling between states of the XAS and non-resonant XES processes can only occur between pairs of the intermediate and final states with nonorthogonal transition moments. Hence, only the *xy*/*xy*- or *z*/*z*-polarized pathways along the two directions may be probed.

(2) Intermediate-state interference provides additional state coupling mechanisms, which allows coupling between intermediate states to the same final states along both polarization pathways. This process generates extra intensity contributions that can be additive or subtractive to the total intensity (eq 14).

DOI: 10.1021/acs.inorgchem.7b01810
Inorg. Chem. 2017, 56, 11819−11836

In an effort to understand the role of the above selection rules, the corresponding XAS and RXES profiles for the $[Mn^{V}N(CN)_4]^{2-}$ complex have been generated at the respective experimental and calculated incident and emission energies. These spectra are visualized in Figures 16 (RXES profiles) and 17 (XAS profiles), respectively, and as can be seen for both RXES and XAS spectra, the calcuated features agree well with the experimental spectra, which is a prerequisite for further analysis.

As is observed in Figure 16, population of the intermediate states that are dominated by the valence 1s → $6a_1$ (1s → $3d_{z^2}$) (~6541 eV) single-electron excitations, results in a Kβ'' and K$\beta_{2,5}$(1,2) pattern that involves solely the *z*-polarized RXES pathway. On the other hand, excitation into the 1s → $6a_1$ (1s → N $2p_z$ and CN σ^*) and 1s → 8e (1s → N $2p_{x,y}$ and CN σ^*) MLCT intermediate states (~6556 eV) results in a Kβ'' and K$\beta_{2,5}$ pattern with a high density of states involving both the *z*- and *xy*-polarized RXES pathways. However, the RXES intensity in this region is subject to interference effects that are either constructive or destructive and amount to about 10% of the total intensity.

The respective experimental XAS spectra generated at constant emission energies (6524, 6529, and 6532 eV; Figure 17) are characterized by significant resonant intensity enhancements in the preedge region. In particular, in the discussion above, it was shown that the coupling between the preedge intermediate XAS and final K$\beta_{2,5}$ RXES states corresponds to the bonding and antibonding counterparts of the σ-type interactions of the manganese center with the nitrido and cyanide ligands (along the *z*- and *xy*-polarized pathways, respectively) results in significant resonance enhancment of the preedge and main-edge XAS regions. The *z*-polarized pathway is shown to dominate the intensity enhancements in the preedge region, while the *xy*-polarized pathway dominates the intensity enhancments in the main-edge region. In contrast to the RXES spectra, the interference contributions to the respective XAS spectra is found to be rather small.

5. CONCLUSIONS

In this paper, we have presented a new protocol to calculate VtC RXES spectra that is based on the DFT/ROCIS method and is firmly grounded in wave-function-based ab initio electronic structure theory. The complete KDH equation has been implemented. The total RIXS cross section can be decomposed into "direct" and "interference" contributions. The overall agreement between the theory and experiment is very good. Furthermore, the calculations allow for a detailed decomposition of the observed spectral features into the contributions of individual excited states and the orbitals that are involved in the transitions. Hence, they also allow detailed correlations to be established between the spectra and geometric and electronic structure. Because the calculations are based on an ab initio method and do not contain elements of data fitting, they can be used to predict the spectra of unknown compounds or to predict the outcome of a measurement on a known compound.

The protocol makes use of the efficient machinery of the DFT/ROCIS method, which has proven to be efficient in treating thousands of many-particle intermediate and final states while at the same time accounting for dynamic correlation and SOC effects. Thus, the new protocol opens the way for addressing many challenging VtC RXES problems that otherwise would remain computationally prohibitive. As a first application of the protocol, we have presented a complete study of the 1s2p VtC RXES problem on the $[Mn^{V}N(CN)_4]^{2-}$ compound. In the presented protocol, the analysis starts by evaluating the non-resonant XAS and XES spectra, by employing both particle−hole-based techniques (one-electron DFT and TD-DFT), as well as the DFT/ROCIS method. These spectra were analyzed with respect to the origin of the dominating multiplet structure. It is shown that SOC effects are essential for the description of both XAS and XES spectra. In addition, at the DFT/ROCIS level, the states that dominate the respective XAS and XES spectra were further analyzed in terms of the predominant single-electron excitations by using the natural orbital transition machinery. In a second step, the complete VtC RXES planes of the $[Mn^{V}N(CN)_4]^{2-}$ complex were evaluated at both the one-electron DFT and DFT/ROCIS levels. A subsequent analysis of the resonant XAS and XES spectra generated at constant emission and incident energies confirmed that the one-electron DFT approach provides a rather simplistic description of the spectra and could not capture the major experimental trends. In contrast, the DFT/ROCIS approach provided very good agreement with the experiment for both the non-resonant and resonant XAS and XES spectra, respectively. Hence, DFT/ROCIS was further evaluated to investigate the intensity mechanism of the above spectra. In particular, we have been able to identify two general and complementary state coupling selection rules of the VtC RXES process that lead to polarized intensity modulations to both XAS and RXES spectra that are not accessible by the TFY XAS or the non-resonant XES process. More specifically, we have been able to explain the complicated experimental pattern of the VtC-detected HFRED spectra. We have shown that the observed enhancements and deenhancements of the preedge spectral feature is a result of a state coupling phenomenon across the two dimensions between the intermediate and final states with nonorthogonal transition moments. Moreover, we have shown that the coupling between the bonding and antibonding counterparts of the final and intermediate states may lead to significant intensity enhancements of the spectral features under resonant conditions. Especially, we have demonstrated that the σ-type bonding and antibonding interactions between the manganese center with the nitrido and cyanide ligands is the source of the preedge feature intensity enhancment of the XAS spectra detected at constant emission energies. Furthermore, intermediate-state interference effects have been shown to be significant, providing contributions of up to 10% of the total intensity of the main edge as well as the K$\beta_{2,5}$ regions of the VtC HERFD XAS and RXES spectra, respectively. This is a result of an additional state coupling mechanism, which involves intermediate states of polarization coupling to the same final states. Taken together, VtC RXES spectroscopy, in combination with wave-function-based protocols, provides a sensitive, accurate, and powerful analysis tool that can probe the electronic structure of molecular and solid systems. More broadly, we hope that the insights obtained in this work are helpful in the design of novel X-ray resonant experiments.[59,60]

■ ASSOCIATED CONTENT

Supporting Information

The Supporting Information is available free of charge on the ACS Publications website at DOI: 10.1021/acs.inorgchem.7b01810.

DOI: 10.1021/acs.inorgchem.7b01810
Inorg. Chem. 2017, 56, 11819−11836

Tables S1 and S2 and Figures S1−S5 as detailed in the text (PDF)

AUTHOR INFORMATION

Corresponding Author

*E-mail: frank.neese@cec.mpg.de.

ORCID

Dimitrios Maganas: 0000-0002-1550-5162

Serena DeBeer: 0000-0002-5196-3400

Notes

The authors declare no competing financial interest.

ACKNOWLEDGMENTS

F.N., S.D., and D.M. acknowledge the Max Planck Society for financial support. S.D. acknowledges funding from the European Research Council under the European Union's Seventh Framework Programme (FP/2007−2013) ERC Grant Agreement 615414. The reviewers of the manuscript are acknowledged for their constructive comments.

REFERENCES

(1) DeBeer George, S.; Neese, F. Calibration of Scalar Relativistic Density Functional Theory for the Calculation of Sulfur K-Edge X-ray Absorption Spectra. *Inorg. Chem.* **2010**, *49* (4), 1849−1853.

(2) Rees, J. A.; Wandzilak, A.; Maganas, D.; Wurster, N. I. C.; Hugenbruch, S.; Kowalska, J. K.; Pollock, C. J.; Lima, F. A.; Finkelstein, K. D.; DeBeer, S. Experimental and theoretical correlations between vanadium K-edge X-ray absorption and Kβ emission spectra. *JBIC, J. Biol. Inorg. Chem.* **2016**, *21*, 793−806.

(3) DeBeer George, S.; Petrenko, T.; Neese, F. Prediction of Iron K-Edge Absorption Spectra Using Time-Dependent Density Functional Theory. *J. Phys. Chem. A* **2008**, *112*, 12936.

(4) Lee, N.; Petrenko, T.; Bergmann, U.; Neese, F.; DeBeer, S. Probing Valence Orbital Composition with Iron Kβ X-ray Emission Spectroscopy. *J. Am. Chem. Soc.* **2010**, *132* (28), 9715−9727.

(5) Roemelt, M.; Maganas, D.; DeBeer, S.; Neese, F. A combined DFT and restricted open-shell configuration interaction method including spin-orbit coupling: application to transition metal L-edge X-ray absorption spectroscopy. *J. Chem. Phys.* **2013**, *138* (20), 204101.

(6) Roemelt, M.; Beckwith, M. A.; Duboc, C.; Collomb, M.-N.; Neese, F.; DeBeer, S. Manganese K-Edge X-Ray Absorption Spectroscopy as a Probe of the Metal−Ligand Interactions in Coordination Compounds. *Inorg. Chem.* **2012**, *51* (1), 680−687.

(7) Lancaster, K. M.; Roemelt, M.; Ettenhuber, P.; Hu, Y.; Ribbe, M. W.; Neese, F.; Bergmann, U.; DeBeer, S. X-ray Emission Spectroscopy Evidences a Central Carbon in the Nitrogenase Iron-Molybdenum Cofactor. *Science* **2011**, *334* (6058), 974−977.

(8) Ament, L. J. P.; van Veenendaal, M.; Devereaux, T. P.; Hill, J. P.; van den Brink, J. Resonant inelastic x-ray scattering studies of elementary excitations. *Rev. Mod. Phys.* **2011**, *83* (2), 705−767.

(9) Solomon, E. I. Spectroscopic Methods in Bioinorganic Chemistry: Blue to Green to Red Copper Sites. *Inorg. Chem.* **2006**, *45* (20), 8012−8025.

(10) de Groot, F. High-Resolution X-ray Emission and X-ray Absorption Spectroscopy. *Chem. Rev.* **2001**, *101* (6), 1779−1808.

(11) de Groot, F. M. F.; Glatzel, P.; Bergmann, U.; van Aken, P. A.; Barrea, R. A.; Klemme, S.; Hävecker, M.; Knop-Gericke, A.; Heijboer, W. M.; Weckhuysen, B. M. 1s2p Resonant Inelastic X-ray Scattering of Iron Oxides. *J. Phys. Chem. B* **2005**, *109* (44), 20751−20762.

(12) Wang, X.; de Groot, F. M. F.; Cramer, S. P. Spin-polarized x-ray emission of 3d transition-metal ions: A comparison via Kα and Kβ detection. *Phys. Rev. B: Condens. Matter Mater. Phys.* **1997**, *56* (8), 4553−4564.

(13) Hämäläinen, K.; Siddons, D. P.; Hastings, J. B.; Berman, L. E. Elimination of the inner-shell lifetime broadening in x-ray-absorption spectroscopy. *Phys. Rev. Lett.* **1991**, *67* (20), 2850−2853.

(14) Hall, E. R.; Pollock, C. J.; Bendix, J.; Collins, T. J.; Glatzel, P.; DeBeer, S. Valence-to-Core-Detected X-ray Absorption Spectroscopy: Targeting Ligand Selectivity. *J. Am. Chem. Soc.* **2014**, *136* (28), 10076−10084.

(15) Josefsson, I.; Kunnus, K.; Schreck, S.; Föhlisch, A.; de Groot, F.; Wernet, P.; Odelius, M. Ab Initio Calculations of X-ray Spectra: Atomic Multiplet and Molecular Orbital Effects in a Multiconfigurational SCF Approach to the L-Edge Spectra of Transition Metal Complexes. *J. Phys. Chem. Lett.* **2012**, *3* (23), 3565−3570.

(16) Schlappa, K.; Wohlfeld, K.; Zhou, J.; Mourigal, M.; Haverkort, M. W.; Strocov, V. N.; Hozoi, L.; Monney, C.; Nishimoto, S.; Singh, S.; Revcolevschi, A.; Caux, J.-S; Patthey, L.; Rønnow, H. M.; van den Brink, J.; Schmitt, a. T. Spin-Orbital Separation in the quasi 1D Mott-insulator Sr2CuO3. *Nature* **2012**, *485*, 82−85.

(17) Guo, M.; Källman, E.; Sørensen, L. K.; Delcey, M. G.; Pinjari, R. V.; Lundberg, M. Molecular Orbital Simulations of Metal 1s2p Resonant Inelastic X-ray Scattering. *J. Phys. Chem. A* **2016**, *120* (29), 5848−5855.

(18) Maganas, D.; Kristiansen, P.; Duda, L.-C.; Knop-Gericke, A.; DeBeer, S.; Schlögl, R.; Neese, F. Combined Experimental and Ab Initio Multireference Configuration Interaction Study of the Resonant Inelastic X-ray Scattering Spectrum of CO_2. *J. Phys. Chem. C* **2014**, *118* (35), 20163−20175.

(19) Wernet, P.; Kunnus, K.; Schreck, S.; Quevedo, W.; Kurian, R.; Techert, S.; de Groot, F. M. F.; Odelius, M.; Föhlisch, A. Dissecting Local Atomic and Intermolecular Interactions of Transition-Metal Ions in Solution with Selective X-ray Spectroscopy. *J. Phys. Chem. Lett.* **2012**, *3* (23), 3448−3453.

(20) Kunnus, K.; Josefsson, I.; Schreck, S.; Quevedo, W.; Miedema, P. S.; Techert, S.; de Groot, F. M. F.; Odelius, M.; Wernet, P.; Föhlisch, A. From Ligand Fields to Molecular Orbitals: Probing the Local Valence Electronic Structure of Ni^{2+} in Aqueous Solution with Resonant Inelastic X-ray Scattering. *J. Phys. Chem. B* **2013**, *117* (51), 16512−16521.

(21) Wernet, P.; Kunnus, K.; Josefsson, I.; Rajkovic, I.; Quevedo, W.; Beye, M.; Schreck, S.; Grubel, S.; Scholz, M.; Nordlund, D.; Zhang, W.; Hartsock, R. W.; Schlotter, W. F.; Turner, J. J.; Kennedy, B.; Hennies, F.; de Groot, F. M. F.; Gaffney, K. J.; Techert, S.; Odelius, M.; Fohlisch, A. Orbital-specific mapping of the ligand exchange dynamics of $Fe(CO)_5$ in solution. *Nature* **2015**, *520* (7545), 78−81.

(22) Bokarev, S. I.; Khan, M.; Abdel-Latif, M. K.; Xiao, J.; Hilal, R.; Aziz, S. G.; Aziz, E. F.; Kühn, O. Unraveling the Electronic Structure of Photocatalytic Manganese Complexes by L-Edge X-ray Spectroscopy. *J. Phys. Chem. C* **2015**, *119* (33), 19192−19200.

(23) Kunnus, K.; Josefsson, I.; Rajkovic, I.; Schreck, S.; Quevedo, W.; Beye, M.; Weniger, C.; Grübel, S.; Scholz, M.; Nordlund, D.; Zhang, W.; Hartsock, R. W.; Gaffney, K. J.; Schlotter, W. F.; Turner, J. J.; Kennedy, B.; Hennies, F.; de Groot, F. M. F.; Techert, S.; Odelius, M.; Wernet, P.; Föhlisch, A. Identification of the dominant photochemical pathways and mechanistic insights to the ultrafast ligand exchange of $Fe(CO)_5$ to $Fe(CO)_4EtOH$. *Struct. Dyn.* **2016**, *3* (4), 043204.

(24) Pollock, C. J.; Delgado-Jaime, M. U.; Atanasov, M.; Neese, F.; DeBeer, S. Kβ Mainline X-ray Emission Spectroscopy as an Experimental Probe of Metal−Ligand Covalency. *J. Am. Chem. Soc.* **2014**, *136* (26), 9453−9463.

(25) Golnak, R.; Bokarev, S. I.; Seidel, R.; Xiao, J.; Grell, G.; Atak, K.; Unger, I.; Thürmer, S.; Aziz, S. G.; Kühn, O.; Winter, B.; Aziz, E. F. Joint Analysis of Radiative and Non-Radiative Electronic Relaxation Upon X-ray Irradiation of Transition Metal Aqueous Solutions. *Sci. Rep.* **2016**, *6*, 24659.

(26) Maganas, D.; Roemelt, M.; Havecker, M.; Trunschke, A.; Knop-Gericke, A.; Schlögl, R.; Neese, F. First principles calculations of the structure and V L-edge X-ray absorption spectra of V2O5 using local pair natural orbital coupled cluster theory and spin-orbit coupled configuration interaction approaches. *Phys. Chem. Chem. Phys.* **2013**, *15* (19), 7260−76.

(27) Roemelt, M.; Neese, F. Excited States of Large Open-Shell Molecules: An Efficient, General, and Spin-Adapted Approach Based

DOI: 10.1021/acs.inorgchem.7b01810
Inorg. Chem. 2017, 56, 11819−11836

on a Restricted Open-Shell Ground State Wave function. *J. Phys. Chem. A* **2013**, *117* (14), 3069−83.
(28) Maganas, D.; Roemelt, M.; Weyhermuller, T.; Blume, R.; Havecker, M.; Knop-Gericke, A.; DeBeer, S.; Schlögl, R.; Neese, F. L-edge X-ray absorption study of mononuclear vanadium complexes and spectral predictions using a restricted open shell configuration interaction ansatz. *Phys. Chem. Chem. Phys.* **2014**, *16* (1), 264−76.
(29) Hess, B. A. Applicability of the no-pair equation with free-particle projection operators to atomic and molecular structure calculations. *Phys. Rev. A: At., Mol., Opt. Phys.* **1985**, *32*, 756.
(30) Hess, B. A. Relativistic electronic-structure calculations employing a two-component no-pair formalism with external-field projection operators. *Phys. Rev. A: At., Mol., Opt. Phys.* **1986**, *33*, 3742.
(31) Jansen, G.; Hess, B. A. Revision of the Douglas-Kroll Transformation. *Phys. Rev. A: At., Mol., Opt. Phys.* **1989**, *39* (11), 6016−6017.
(32) Douglas, M.; Kroll, N. M. Quantum electrodynamical corrections to the fine structure of helium. *Ann. Phys.* **1974**, *82* (1), 89−155.
(33) Wolf, A.; Reiher, M.; Hess, B. A. The generalized Douglas−Kroll transformation. *J. Chem. Phys.* **2002**, *117* (20), 9215−9226.
(34) Lenthe, E. v.; Baerends, E. J.; Snijders, J. G. Relativistic regular two-component Hamiltonians. *J. Chem. Phys.* **1993**, *99* (6), 4597−4610.
(35) van Lenthe, E.; van der Avoird, A.; Wormer, P. E. S. Density functional calculations of molecular hyperfine interactions in the zero order regular approximation for relativistic effects. *J. Chem. Phys.* **1998**, *108* (12), 4783−4796.
(36) Heully, J. L.; Lindgren, I.; Lindroth, E.; Lundqvist, S.; Martensson-Pendrill, A. M. Diagonalisation of the Dirac Hamiltonian as a basis for a relativistic many-body procedure. *J. Phys. B: At. Mol. Phys.* **1986**, *19* (18), 2799.
(37) Neese, F. Efficient and accurate approximations to the molecular spin-orbit coupling operator and their use in molecular g-tensor calculations. *J. Chem. Phys.* **2005**, *122* (3), 034107.
(38) Atanasov, M.; Aravena, D.; Suturina, E.; Bill, E.; Maganas, D.; Neese, F. First principles approach to the electronic structure, magnetic anisotropy and spin relaxation in mononuclear 3d-transition metal single molecule magnets. *Coord. Chem. Rev.* **2015**, *289−290*, 177−214.
(39) Yano, J.; Robblee, J.; Pushkar, Y.; Marcus, M. A.; Bendix, J.; Workman, J. M.; Collins, T. J.; Solomon, E. I.; DeBeer George, S.; Yachandra, V. K. Polarized X-ray Absorption Spectroscopy of Single-Crystal Mn(V) Complexes Relevant to the Oxygen-Evolving Complex of Photosystem II. *J. Am. Chem. Soc.* **2007**, *129* (43), 12989−13000.
(40) Kramers, H. A.; Heisenberg, W. On the dispersal of radiation by atoms. *Z. Phys.* **1925**, *31*, 681−708.
(41) Neese, F.; Petrenko, T.; Ganyushin, D.; Olbrich, G. Advanced aspects of ab initio theoretical optical spectroscopy of transition metal complexes: Multiplets, spin-orbit coupling and resonance Raman intensities. *Coord. Chem. Rev.* **2007**, *251* (3−4), 288−327.
(42) Neese, F. The ORCA program system. *Wiley Interdiscip. Rev. Comput. Mol. Sci.* **2012**, *2* (1), 73−78.
(43) Perdew, J. P. Density-Functional Approximation for the Correlation-Energy of the Inhomogeneous Electron-Gas. *Phys. Rev. B: Condens. Matter Mater. Phys.* **1986**, *33* (12), 8822−8824.
(44) Becke, A. D. Density-functional exchange-energy approximation with correct asymptotic-bahaviour. *Phys. Rev. A: At., Mol., Opt. Phys.* **1988**, *38* (6), 3098−3100.
(45) Becke, A. D. Density-functional thermochemistry. III. The role of exact exchange. *J. Chem. Phys.* **1993**, *98*, 5648.
(46) Lee, C.; Yang, W.; Parr, R. G. Development of the Colle-Salvetti correlation-energy formula into a functional of the electron densit. *Phys. Rev. B: Condens. Matter Mater. Phys.* **1988**, *37*, 785.
(47) Grimme, S.; Antony, J.; Ehrlich, S.; Krieg, H. A consistent and accurate ab initio parametrization of density functional dispersion correction (DFT-D) for the 94 elements H-Pu. *J. Chem. Phys.* **2010**, *132* (15), 154104.
(48) Grimme, S.; Ehrlich, S.; Goerigk, L. Effect of the damping function in dispersion corrected density functional theory. *J. Comput. Chem.* **2011**, *32* (7), 1456−1465.
(49) Feyereisen, M.; Fitzgerald, G.; Komornicki, A. Use of approximate integrals in ab initio theory. An application in MP2 energy calculations. *Chem. Phys. Lett.* **1993**, *208*, 359.
(50) Kendall, R. A.; Fruchtl, H. A. The impact of the resolution of the identity approximate integral method on modern ab initio algorithm development. *Theor. Chem. Acc.* **1997**, *97* (1−4), 158−163.
(51) Neese, F. Importance of Direct Spin−Spin Coupling and Spin-Flip Excitations for the Zero-Field Splittings of Transition Metal Complexes: A Case Study. *J. Am. Chem. Soc.* **2006**, *128* (31), 10213−10222.
(52) Maganas, D.; DeBeer, S.; Neese, F. Restricted Open-Shell Configuration Interaction Cluster Calculations of the L-Edge X-ray Absorption Study of TiO2 and CaF2 Solids. *Inorg. Chem.* **2014**, *53* (13), 6374−6385.
(53) Bergmann, U.; Bendix, J.; Glatzel, P.; Gray, H. B.; Cramer, S. P. Anisotropic valence→core x-ray fluorescence from a $[Rh(en)_3][Mn(N)(CN)_5]\cdot H_2O$ single crystal: Experimental results and density functional calculations. *J. Chem. Phys.* **2002**, *116* (5), 2011−2015.
(54) Marchenko, T.; Carniato, S.; Journel, L.; Guillemin, R.; Kawerk, E.; Žitnik, M.; Kavčič, M.; Bučar, K.; Bohinc, R.; Petric, M.; Vaz da Cruz, V.; Gel'mukhanov, F.; Simon, M. Electron Dynamics in the Core-Excited CS_2 Molecule Revealed through Resonant Inelastic X-Ray Scattering Spectroscopy. *Phys. Rev. X* **2015**, *5* (3), 031021.
(55) Sun, Y. P.; Miao, Q.; Pietzsch, A.; Hennies, F.; Schmitt, T.; Strocov, V. N.; Andersson, J.; Kennedy, B.; Schlappa, J.; Föhlisch, A.; Gel'mukhanov, F.; Rubensson, J. E. Interference between Resonant and Non-resonant Inelastic X-Ray Scattering. *Phys. Rev. Lett.* **2013**, *110* (22), 223001.
(56) Neese, F.; Hedman, B.; Hodgson, K. O.; Solomon, E. I. Relationship between the Dipole Strength of Ligand Pre-Edge Transitions and Metal−Ligand Covalency. *Inorg. Chem.* **1999**, *38* (21), 4854−4860.
(57) Neese, F.; Solomon, E. I. MCD C-Term Signs, Saturation Behavior, and Determination of Band Polarizations in Randomly Oriented Systems with Spin $S \geq 1/2$. Applications to $S = 1/2$ and $S = 5/2$. *Inorg. Chem.* **1999**, *38* (8), 1847−1865.
(58) Ye, S.; Kupper, C.; Meyer, S.; Andris, E.; Navrátil, R.; Krahe, O.; Mondal, B.; Atanasov, M.; Bill, E.; Roithová, J.; Meyer, F.; Neese, F. Magnetic Circular Dichroism Evidence for an Unusual Electronic Structure of a Tetracarbene−Oxoiron(IV) Complex. *J. Am. Chem. Soc.* **2016**, *138* (43), 14312−14325.
(59) Lieutenant, K.; Hofmann, T.; Schulz, C.; Yablonskikh, M. V.; Habicht, K.; Aziz, E. F. Design concept of the high-resolution end-station PEAXIS at BESSY II: Wide-Q-range RIXS and XPS measurements on solids, solutions, and interfaces. *J. Electron Spectrosc. Relat. Phenom.* **2016**, *210*, 54−65.
(60) Van Kuiken, B. E.; Hahn, A. W.; Maganas, D.; DeBeer, S. Measuring Spin-Allowed and Spin-Forbidden d−d Excitations in Vanadium Complexes with 2p3d Resonant Inelastic X-ray Scattering. *Inorg. Chem.* **2016**, *55* (21), 11497−11501.

DOI: 10.1021/acs.inorgchem.7b01810
Inorg. Chem. 2017, 56, 11819−11836